INTERNATIONAL JOURNAL FOR NUMERICAL METHODS IN ENGINEERING
Int. J. Numer. Meth. Engng 0000; **00**:1–34
Published online in Wiley InterScience (www.interscience.wiley.com). DOI: 10.1002/nme

A micro-mechanics-based inverse study for stochastic order reduction of elastic UD-fiber reinforced composites analyzes

L. Wu[1*], L. Adam[2] and L. Noels[1]

[1] *University of Liege, Department of Aeronautics and Mechanical Engineering, Computational & Multiscale Mechanics of Materials, Allée de la découverte 9, B-4000 Liège, Belgium*
[2] *e-Xstream Engineering, Axis Park-Building H, Rue Emile Francqui 9, B-1435 Mont-Saint-Guibert, Belgium*

SUMMARY

This research develops a stochastic mean-field-homogenization (MFH) process that is used as Reduced Order Model (ROM) to carry out a statistical multiscale analysis on unidirectional (UD) fiber reinforced composites. First full-field simulations of UD Stochastic Volume Elements (SVEs), whose statistical description is obtained from SEM images, are conducted to define statistical meso-scale apparent properties. A stochastic Mori-Tanaka MFH model is then developed through an inverse stochastic identification process performed on the apparent elastic properties obtained by full-field simulations. As a result, a random vector of the effective elastic properties of phases and micro-structure information of the Mori-Tanaka model is inferred. In order to conduct Stochastic Finite Element Method (SFEM) analyzes, a generator of this random vector is then constructed using the copula method, allowing predicting the statistical response of a composite ply under bending. The statistical dependence of the random vector entries is shown to be respected by the generator. Although this work is limited to the elastic response, we believe that the stochastic Mori-Tanaka model can be extended to nonlinear behaviors in order to conduct efficient stochastic multiscale simulations. Copyright © 0000 John Wiley & Sons, Ltd.

Received . . .

KEY WORDS: Multiscale; Stochastic problems; Order reduction; Mean-Field Homogenization; Composites

1. INTRODUCTION

Nowadays, the models developed in science and engineering practices are of increasing complexity, and the solutions of these models can only be acquired via numerical methods most of the time. Taking advantage from the ability of computers which develop at high speed, numerical analyzes and simulations are applied to a broad range of applications. However, computational power is limited, and the simulations of detailed models or analyzes that require a large number of simulations cannot always been achieved. This is the case in the context of modeling of composite

*Correspondence to: L. Wu, University of Liège, A&M-CM3, B52 Quartier Polytech 1, Allée de la Dćouverte 9, B4000 Liège, Belgium, Phone: +32 4 366 94 53, E-mail: L.Wu@ulg.ac.be

materials, for which numerical methods can lead to massive discretizations depending on the involved phases and their geometrical arrangements. This problem becomes even more severe when uncertainties are considered and Monte Carlo (MC) methods are required for statistical analyzes.

In order to carry out a complex analysis at an affordable computational cost, various approaches have been developed in the field of Reduced Order Model (ROM). Widely speaking, any method which helps to reduce the size or complexity of a numerical system, which needs to be solved, is an order reduction.

The purpose of this research is to carry out a statistical multiscale analysis on unidirectional (UD) fiber reinforced composites, in which case the model order reduction has a twofold meaning: the first one is in the sense of stochastic analysis; and the second one is in the sense of a (deterministic) multiscale analysis.

In a stochastic analysis, order reductions, which aim at reducing the stochastic dimension of the random quantities used in the stochastic modeling of uncertain parameters and of the random observations in a computational model, are called statistical reduction. Such a statistical reduction is also used in the stochastic modeling of data coming from experimental measurements and/or from numerical simulations. For second-order random variables or random fields for which the covariance matrix is known, there are two well documented tools for statistical reduction: the first one is the principal component analysis (PCA), which can deal with the statistical reduction of a random vector $\mathcal{V}$ in finite dimension; and the second one is the Karhunen-Loève expansion which can handle the statistical reduction of a random field $\mathcal{F}$ in infinite dimension.

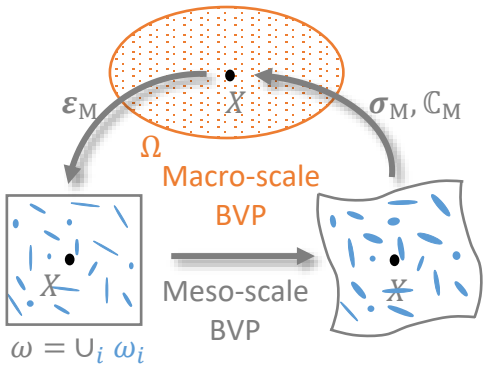

Figure 1. Definition of the homogenization method performed on the meso-scale volume element ω.

Homogenization-based multiscale analyzes have been extensively developed, see the reviews [1, 2, 3]. In particular FE^2 strategies [4, 5, 6, 7, 8] have gained popularity with the increase in computational power. In such an approach, the macro-scale structure defines a Boundary Value Problem (BVP) which is solved by considering homogenized material properties extracted, at each (macro) material point of interest, from the resolution of a meso-scale BVP, see Fig. 1. This meso-scale BVP is defined on a meso-scale volume, which represents the different phases of the material. Some homogenization methods investigate the response of meso-scale volume elements through full-field analyzes, which limits the applicability of the multiscale simulations to reduced size problems. The researches on ROM aim at providing an efficient homogenization process with a reduced version of the full-field analyzes. With the general idea of trading space for time, the ROM

DOI: 10.1002/nme

is mainly based on pre-off-line computations. In micro-scale analyzes, reduced versions of models are created by projection of the governing equations into suitably selected sub-spaces based on the acquired information from pre-off-line computations on a meso-scale volume. The micro-scale model could be a computational model with a large number of displacement degrees of freedom, such as in the FE^2 method, in which case the reduced number of unknown variables is defined by means of proper orthogonal decomposition of the displacement field [9]. A further order reduction, called hyper-reduction, can be applied to reduce the computations on internal forces [10, 11]. A numerical comparison of different projection-based ROMs in computational homogenization can be found in [11]. The micro-scale ROM could also be a mechanical model that involves much less variables, such as in micro-mechanics: order reduction is achieved in the nonuniform transformation field analysis (NTFA) by using the pre-defined internal variables modes obtained with a full-field FE analysis [12], and a tangent second-order (TSO) expansion of the dissipation potential is adopted to speedup simulations [13]. The pre-off-line computations can also provide surrogate models by means of constructing mapping functions, such as through kernel methods [14], polynomial chaos expansion [15] etc.

These ROMs are mainly applied to deterministic multiscale analyzes. In this case, a statistical representative meso-scale volume element, which is called Representative Volume Element (RVE), is used in the full-field analysis. When uncertainties are involved, or when the volume element is not several order of magnitude larger than the micro-scale size, the meso-scale volume element does not respect the statistical representativity and is called Statistical or Stochastic Volume Element (SVE) [16]. Therefore, the homogenized response depends on the SVE realization, and on the applied boundary conditions as discussed for 2D-particle reinforced composites in the case of elasticity [17, 18], linear micro-polar continua [19, 20, 21], elastoplasticity [17], thermoelasticity or again finite elasticity [17]. For a given type of boundary condition, the homogenized properties of SVE realizations exhibit a distribution whose standard deviation increases when the SVE size becomes closer to the inclusion size. It has also been shown in [17] that the discrepancy is more important in nonlinear cases than in linear elasticity. In the latter references, average properties obtained using successively constrained displacement and traction boundary conditions –considered as two bounding cases– on SVEs of different sizes were used to define the minimum SVE size allowing statistically representative (and thus unique) homogenized properties to be extracted as the bounds average. However stochastic homogenization can also be applied to capture the variation in the homogenized response with a view of upscaling the resulting uncertainties. In this context, computational homogenization performed on SVEs results in statistical homogenized properties of heterogeneous materials: the homogenized behavior of random two-phase elastic composites was described by a transverse isotropic law with resultant Young's modulus and Poisson ratio [22, 23, 24], an orthogonal anisotropic law was adopted in [25] for the same material system and in [26] and [27] for polysilicon elastic behavior and thermoelastic damping, respectively. In the context of nonlinear materials, a complete statistical analysis combining Monte Carlo (MC) resolutions of SVEs to multiscale analyzes would require a huge series of pre-off-line computations on SVEs. Moreover, the requirement of memory to store the information from off-line computations will become overwhelming. An economical practice to avoid the costly coupled micro-scale computations and the storage of pre-off-line information is to stochastically calibrate a phenomenological macroscopic model with homogenized responses from full-field simulations

DOI: 10.1002/nme

performed on SVEs. However, the choice of the macroscopic model could be arbitrary and it is not always easy to find a well fitted model when the materials system obeys to a complex behavior. Moreover the information provided by the full-field simulations is discarded. These limitations have motivated the research on the subject of efficient stochastic multiscale analyzes. In [28], the stochastic homogenization of a UD composite cell is achieved by using a modified version of the meso-scale Stochastic Finite Element Method (SFEM), leading to a more efficient solution. In [29], stochastic multiscale analyzes were developed to account for fine-scale material properties as random variables –and random fields in particular cases– using an order reduction method combined to an asymptotic homogenization relying on the use of SVEs. In the context of finite elasticity, a ROM was built from the resolution of SVEs, which are called composite material elementary cells, by defining a meso-scale potential capturing the uncertainties related to the fibers geometry/distribution in composites [30, 31]. In a more general way, the use of ROMs in data-driven nonlinear stochastic analyzes is discussed in [32].

In this work, we propose to use a micro-mechanics-based ROM in which the effective constitutive parameters of the different phases are stochastically calibrated from SVE full-field resolutions. Considering inclusion reinforced matrix composites, Mean Field Homogenization (MFH), in particular the Mori-Tanaka Method [33], is chosen as the micro-mechanics model. Although in this work we focus on the linear response of unidirectional composite materials as a first step, with a view to nonlinear and failure studies, the interest of the Mori-Tanaka Method lies in its ability to represent complex nonlinear composite material behaviors, including failure [34], in an accurate way. In contrast to the computational homogenization method, the RVE or SVE in MFH is only a concept: there are no realizations of RVEs/SVEs being used during the homogenization. As a result, MFH cannot directly capture the micro-structure uncertainty effects. Therefore, the overall effect of micro-structure uncertainties needs to be represented by some key parameters as random variables in MFH analyzes. To identify and evaluate these key parameters, an inverse Mori-Tanaka analysis can be used. The inverse Mori-Tanaka analysis has been used to identify the material constants of effective matrix of nanocomposites with the overall mechanical behavior of nanocomposites given by molecular dynamics simulations [35], and to perform the convergence analysis of material parameters of effective matrix according to the size of RVE [36]. In the present work, the effective elastic properties of phases and micro-structure information of the MFH micro-mechanics model are identified in a stochastic way by an inverse Mori-Tanaka process conducted on the results of computational full-field analyzes of SVE realizations. Since each SVE realization yields one set of parameters –the effective elastic properties of phases and micro-structure information– of the MFH micro-mechanics model, the latter corresponds to a realization of a random vector $\mathcal{V}_{\text{M-T}}$. This random vector $\mathcal{V}_{\text{M-T}}$, which is evaluated by repeating the inverse identification process on several SVE realizations, thus defines the input of the stochastic Mori-Tanaka ROM.

Conducting multiscale simulations using the Mori-Tanaka model has several advantages: the homogenized response of the composite material is obtained at a low computational cost even for nonlinear simulations, complicated anisotropic damage evolutions usually considered in the case of damage simulations are replaced by simple isotropic damage laws in the phases [37, 38], and finally, although the detailed information provided by the full-field simulations is lost, a certain amount of qualitative information is kept by the micro-mechanics model in the sense of volume average. These advantages make the stochastic Mori-Tanaka model an efficient ROM to achieve

DOI: 10.1002/nme

a full process from micro-structure analysis to statistical evaluation of composite structures. To this end, the stochastic scale-transition, involved in propagating the uncertainties at the meso-scale (SVEs) to the macro-structural scale, is carried out by SFEM. Therefore, by using material properties which are random, SFEM can propagate the uncertainties through the mechanical system and assess the structural stochastic response [39, 16, 40, 41]. In the present work, the random vector $\mathcal{V}_{\text{M-T}}$ of the effective elastic properties of phases and micro-structure information of the Mori-Tanaka model corresponds to the random properties of the SFEM. Therefore, in order to conduct the SFEM analyzes, a generator of the random vector is constructed using the copula method [42].

However, conducting a reliable stochastic multiscale structural analysis by SFEM requires the stochastic description of the material properties to be defined accounting for the size of the stochastic finite elements [26]: the SVEs used to define the meso-scale random material property fields should have a comparable size to the finite element size in the composite structure analysis. Since there exists a huge length gap between the computationally affordable SVEs size to the finite element size of structural analysis in UD-fiber reinforced composites, the multi-level computational stochastic homogenization developed in [25] is considered to define the random vector $\mathcal{V}_{\text{M-T}}$. However, no ROM was developed in [25], which is the purpose of the present work through the development of an inverse stochastic identification of the Mori-Tanaka model.

The paper is organized as follows. In Section 2, the stochastic homogenization of UD SVEs is conducted, using as input the statistical description obtained from SEM images in [25]. In particular the statistical convergence of the homogenized apparent elastic properties is studied. The stochastic Mori-Tanaka model is developed in linear elasticity in Section 3. To this end, an inverse stochastic identification process is performed from the apparent elastic properties in order to define the random vector $\mathcal{V}_{\text{M-T}}$ of the effective elastic properties of phases and micro-structure information of the Mori-Tanaka model. The statistical dependence of this vector entries is also studied. The cumulative distributions of the apparent elastic properties obtained by the stochastic Mori-Tanaka model are compared to the results of the stochastic full-field homogenization in Section 4. A good agreement between the two homogenization processes is found and confirmed by studying macro-scale SFEM of a single composite ply realization. Finally, the dimension obtained by applying an order reduction using a PCA on the random vector $\mathcal{V}$ obtained directly by the computational stochastic homogenization is shown to be equivalent to the dimension of the random vector $\mathcal{V}_{\text{M-T}}$. In order to conduct SFEM, a generator of the random vector $\mathcal{V}_{\text{M-T}}$ is constructed using the copula method [42] in Section 5. The statistical dependence of the random vector entries is shown to be respected by the generator. A SFEM analysis of a composite ply under bending is then conducted to demonstrate the applicability of the method. Finally, conclusions are drawn in Section 6.

2. STATISTICAL ANALYSIS OF THE APPARENT –OR HOMOGENIZED– MESO-SCALE MATERIAL PROPERTIES BASED ON SVES

The statistical analysis of the apparent meso-scale material properties is carried out based on the generated Stochastic Volume Elements (SVEs). With a proper micro-structure generation scheme, which keeps the spatial characteristics of micro-structures, an adequate number of virtual samples –here the SVEs– can be generated for virtual tests –here homogenizations. In this section, we briefly

DOI: 10.1002/nme

summarize the SVE generation process built from SEM images statistical analysis as developed in [25] and the computational homogenization theory. Stochastic homogenization is then applied on the generated SVEs, and, using the obtained probabilistic behavior of the homogenized meso-scale material, a classical statistical procedure, the Principal Component Analysis (PCA), is performed. Finally, the aspect of random variables dimensionality reduction is discussed with a view to the generation of random meso-scale material property.

2.1. Definition of the SVEs

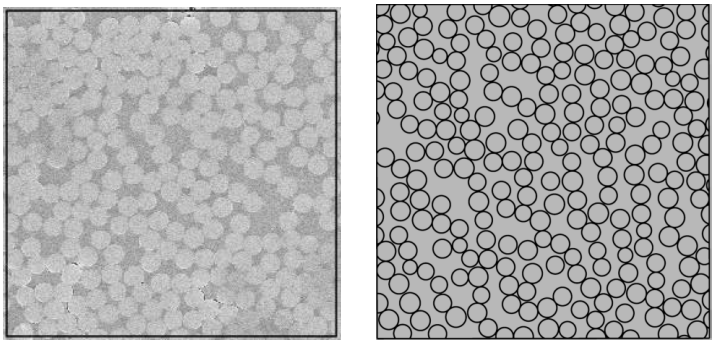

(a) SEM image (b) Numerical model

Figure 2. Micro-structures of UD-fiber reinforced composite [25]: (a) cross-section SEM image; (b) Generated micro-structure.

In this work, we consider SVEs of UD composite materials in which the uncertainties result from the fiber radius and spatial distribution. The micro-structure of UD carbon fiber reinforced composites was statistically studied from cross-section SEM images in [25], in which a numerical micro-structure model was developed. The numerical micro-structure model is built on the images spatial analysis; empirical statistical descriptors are considered as dependent variables and represented using the copula framework. Numerical micro-structures are then generated from numerical sampling of these random variables combined to a fibers additive process. As a result, the micro-structure realizations have an equivalent random fiber radius distribution and an equivalent spatial distribution of fibers as the real composite material, see Fig. 2 which compares an SEM image to a generated micro-structure. Note that the fibers packing was observed to be more dense along the ply-thickness direction than along the ply width, and this feature is respected by the generation process [25].

SVE cross-sections are then extracted from the numerical micro-structure realizations using a square window of length l_{SVE}, see an example of a realization with $l_{\mathrm{SVE}} = 25\,\mu$m in Fig. 3. Since the SVEs are extracted from a larger micro-structure, fibers that cut the window are naturally considered, improving the accuracy of the homogenization as compared to unrealistic volume elements in which inclusions are constrained not to cross the window edges, see the discussion in [20]. A 3D model is then obtained by extruding the extracted 2D cross-section along the longitudinal direction “L” of the fibers, which also refers to the z-direction in this work. The transverse directions “T” and “T’ ” of the fibers refer to the x- and y-directions, respectively, with y along the thickness direction of the laminate, see Fig. 3(a).

Prepared using nmeauth.cls
DOI: 10.1002/nme

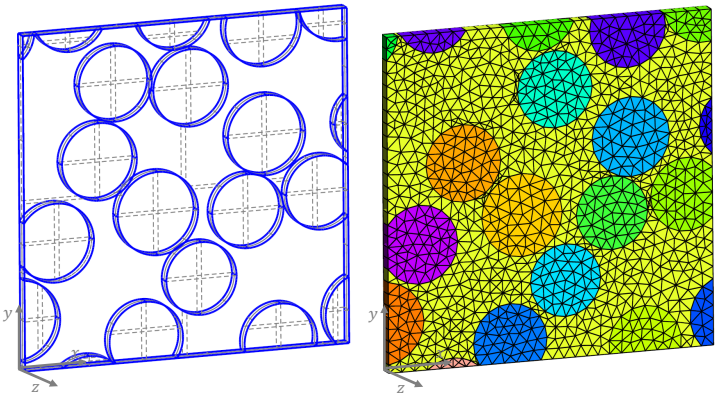

(a) (b)

Figure 3. Example of a $25 \times 25 \times 1 \mu\text{m}^3$ meso-scale volume element: (a) geometry of a SVE realization; and (b) finite element discretization of the SVE.

The properties of matrix and fibers are assumed to be respectively isotropic linear elastic and transverse isotropic linear elastic. As an assumption the micro-scale material properties are assumed not to suffer from uncertainties. A similar material system has been identified and used in [38, 25], in which the elastic properties of the matrix and fibers are:

- Matrix: Elastic Young's modulus $E_0 = 3.2$ GPa; Poisson ratio $\nu_0 = 0.3$.
- Inclusions (fibers): Longitudinal Young's modulus $E_{\text{I}}^{\text{L}} = 230$ GPa; transverse Young's modulus $E_{\text{I}}^{\text{T}} = 40$ GPa; transverse Poisson ratio $\nu_{\text{I}}^{\text{TT}} = 0.2$; longitudinal-transverse Poisson ratio $\nu_{\text{I}}^{\text{LT}} = 0.256$; transverse shear modulus $G_{\text{I}}^{\text{TT}} = 16.7$ GPa; longitudinal-transverse shear modulus $G_{\text{I}}^{\text{LT}} = 24$ GPa.

Since the windows used to extract the micro-structures do not allow to reach statistical representativity, the homogenized elastic properties depend on the SVE realization, and on the applied boundary conditions as discussed in the introduction. The fact that the homogenized properties are not unique has been exploited in the context of polycrystal in [26] to predict the stochastic response at the structural scale. In particular, several SVE sizes have been studied and it has been shown that, although the homogenized properties distributions depend on this size, the distribution of the macro-scale or structural response is not dependent on the SVE size providing the following three conditions are fulfilled:

1. The size of the SVE remains small compared to the structural scale;
2. The macro-scale simulations rely on the SFEM using as input a random field defined from the homogenized properties distributions and their spatial correlations;
3. The size of the stochastic finite elements used at the macro-scale is smaller than the correlation length of this random field; Note that this correlation length increases with the SVE size.

The effect of the SVE size has also been investigated in the case of UD composites [25]. For the considered micro-structure, it has been shown that for SVEs of length $l_{\text{SVE}} \geq 25\ \mu$m, the distribution of the homogenized elastic properties gets close to a normal distribution and the auto/cross correlation vanishes at a distance equal to the SVE length. In other words, for two neighboring SVEs, although they may share some common fibers, their homogenized elastic properties are not

DOI: 10.1002/nme

correlated and the homogenized properties can be approximated as independent random vectors. Therefore, in this work we consider the size $l_{\mathrm{SVE}} \geq 25\,\mu$m, and as a result

1. SVEs can be independently generated micro-structures;
2. The SVEs spatial correlation does not have to be considered;
3. The SFEM at the higher scale will use a random field discretized by a grid of $25\,\mu$m-spacing, unless a second step homogenization is performed as discussed in Section 5.2.

2.2. Evaluation of the apparent elastic properties of SVEs with computational homogenization

The apparent meso-scale material tensor can be estimated from the resolution of the meso-scale boundary value problem (BVP) solved with the finite element method [7, 43]. The so-called computational homogenization method is summarized in the context of linear elasticity in this section. In particular, periodical boundary condition is applied on the meso-scale volume element and the extraction of the homogenized material operator follows the multiple-constraint projection method [44] detailed in [45].

2.2.1. The meso-scale Boundary Value Problem (BVP) The meso-scale BVP is defined on the meso-scale volume element: an SVE ω of boundary $\partial\omega$, see Fig. 1. Since the SVE size is rather small, here typically $25 \times 25 \times 1\mu\mathrm{m}^3$, the time of the stress wave to propagate in the SVE remains negligible. Therefore, the equivalence of the micro-strain to the macro-strain is instantaneous and the equilibrium equations read

$$\begin{cases} \nabla_{\mathrm{m}} \cdot \boldsymbol{\sigma}_{\mathrm{m}} = \mathbf{0} & \forall \boldsymbol{x} \in \omega\,, \\ \boldsymbol{n}_{\mathrm{m}} \cdot \boldsymbol{\sigma}_{\mathrm{m}} = \boldsymbol{t}_{\mathrm{m}} & \forall \boldsymbol{x} \in \partial\omega\,, \end{cases} \tag{1}$$

where the subscript 'm' refers to the local value at the micro-scale, $\boldsymbol{\sigma}_{\mathrm{m}}$ is the Cauchy stress tensor, and $\boldsymbol{t}_{\mathrm{m}}$ is the surface traction on the boundary of outward unit normal $\boldsymbol{n}_{\mathrm{m}}$. Notations are given in Appendix A.

To complete the micro-scale problem, the local constitutive laws of the different materials are assumed to follow linear elasticity in this work, leading to

$$\boldsymbol{\sigma}_{\mathrm{m}} = \mathbb{C}_{\mathrm{m}}\left(\boldsymbol{x}\right) : \boldsymbol{\varepsilon}_{\mathrm{m}}\,, \tag{2}$$

where the fourth-order material tensor $\mathbb{C}_{\mathrm{m}}\left(\boldsymbol{x}\right)$ depends on the micro-scale material point location $\boldsymbol{x}$, and the small-deformation strain tensor $\boldsymbol{\varepsilon}_{\mathrm{m}}$ is evaluated in terms of the micro-scale displacement $\boldsymbol{u}_{\mathrm{m}}$ as $\boldsymbol{\varepsilon}_{\mathrm{m}} = \frac{1}{2}\left(\nabla_{\mathrm{m}} \otimes \boldsymbol{u}_{\mathrm{m}} + \boldsymbol{u}_{\mathrm{m}} \otimes \nabla_{\mathrm{m}}\right)$.

2.2.2. The scale transition The volume average of a micro-scale field on the meso-scale volume-element ω is written as

$$\cdot_{\mathrm{M}} = <\cdot_{\mathrm{m}}> = \frac{1}{V(\omega)} \int_{\omega} \cdot_{\mathrm{m}} \mathrm{d}V\,, \tag{3}$$

where $\langle\cdot\rangle$ is the volume average of the field $\cdot$, and $V(\omega)$ is the volume of the meso-scale volume element ω, the resulting value is defined as the homogenized value with the subscript 'M'.

DOI: 10.1002/nme

In general, the apparent fourth-order material tensor, $\mathbb{C}_{\mathrm{M}}$, is not the volume average of $\mathbb{C}_{\mathrm{m}}$. Instead, it is defined in order to ensure the energy consistency at the different scales, which corresponds to the Hill-Mandel condition

$$\boldsymbol{\sigma}_{\mathrm{M}} : \delta\boldsymbol{\varepsilon}_{\mathrm{M}} = \delta\boldsymbol{\varepsilon}_{\mathrm{M}} : \mathbb{C}_{\mathrm{M}} : \boldsymbol{\varepsilon}_{\mathrm{M}} =< \delta\boldsymbol{\varepsilon}_{\mathrm{m}} : \mathbb{C}_{\mathrm{m}} : \boldsymbol{\varepsilon}_{\mathrm{m}} > , \tag{4}$$

where $\boldsymbol{\sigma}_{\mathrm{M}}$ and $\boldsymbol{\varepsilon}_{\mathrm{M}}$ are the homogenized stress and strain tensors, respectively. In particular, in the context of linear elasticity, we have

$$\begin{cases} \boldsymbol{\sigma}_{\mathrm{M}} =< \boldsymbol{\sigma}_{\mathrm{m}} >=< \mathbb{C}_{\mathrm{m}} : \boldsymbol{\varepsilon}_{\mathrm{m}} >= \mathbb{C}_{\mathrm{M}} : \boldsymbol{\varepsilon}_{\mathrm{M}} , \\ \boldsymbol{\varepsilon}_{\mathrm{M}} = \left(\frac{\nabla_{\mathrm{M}} \otimes \boldsymbol{u}_{\mathrm{M}} + \boldsymbol{u}_{\mathrm{M}} \otimes \nabla_{\mathrm{M}}}{2} \right) =< \boldsymbol{\varepsilon}_{\mathrm{m}} > , \end{cases} \tag{5}$$

where $\boldsymbol{u}_{\mathrm{M}}$ is the macro-scale displacement field.

In order to satisfy this energy consistency condition, the scale transition problem is completed by a specially defined boundary conditions applied on the meso-scale volume element ω. To this end, the micro-scale displacement field is written under the form

$$\boldsymbol{u}_{\mathrm{m}}(\boldsymbol{x}) = (\boldsymbol{u}_{\mathrm{M}} \otimes \nabla_{\mathrm{M}}) \cdot (\boldsymbol{x} - \boldsymbol{x}_{\mathrm{ref}}) + \boldsymbol{u}'(\boldsymbol{x}) , \tag{6}$$

where $\boldsymbol{x}_{\mathrm{ref}}$ is a reference point of ω and $\boldsymbol{u}'$ is the perturbation field. The definition of the homogenized strain, Eq. (5), requires this perturbation field to satisfy

$$0 =< \boldsymbol{u}'(\boldsymbol{x}) \otimes \nabla_{\mathrm{m}} >= \frac{1}{V(\omega)} \int_{\partial\omega} \boldsymbol{u}' \otimes \boldsymbol{n}_{\mathrm{m}} \mathrm{d}S . \tag{7}$$

Moreover, by substituting Eq. (6) in Eq. (4), integrating by parts, and using the equilibrium Eqs. (1), the Hill-Mandel condition can be rewritten as

$$\boldsymbol{\sigma}_{\mathrm{M}} : \delta\boldsymbol{\varepsilon}_{\mathrm{M}} =< \boldsymbol{\sigma}_{\mathrm{m}} : \delta\boldsymbol{\varepsilon}_{\mathrm{m}} >= \boldsymbol{\sigma}_{\mathrm{M}} : \delta\boldsymbol{\varepsilon}_{\mathrm{M}} + \frac{1}{V(\omega)} \int_{\omega} \boldsymbol{\sigma}_{\mathrm{m}} : (\delta\boldsymbol{u}' \otimes \nabla_{\mathrm{m}}) \mathrm{d}V , \tag{8}$$

or again as

$$0 = \frac{1}{V(\omega)} \int_{\partial\omega} (\boldsymbol{\sigma}_{\mathrm{m}} \cdot \boldsymbol{n}_{\mathrm{m}}) \cdot \delta\boldsymbol{u}' \mathrm{d}S = \int_{\partial\omega} \boldsymbol{t}_{\mathrm{m}} \cdot \delta\boldsymbol{u}' \mathrm{d}S . \tag{9}$$

2.2.3. Definition of the constrained micro-scale finite element problem The weak form of the micro-scale Eqs. (1) reads

$$\int_{\omega} \boldsymbol{\sigma}_{\mathrm{m}} : (\delta\boldsymbol{u}' \otimes \nabla_{\mathrm{m}}) \mathrm{d}V = 0 , \quad \forall \delta\boldsymbol{u}' \in \mathcal{U} , \tag{10}$$

where $\mathcal{U}$ is the admissible kinematic vector field defined as a subset of the minimum kinematic field $\mathcal{U}^{\min}$ satisfying Eq. (7):

$$\mathcal{U}^{\min} = \left\{ \boldsymbol{u}' | \int_{\partial\omega} \boldsymbol{u}' \otimes \boldsymbol{n}_{\mathrm{m}} \mathrm{d}S = 0 \right\} . \tag{11}$$

In that case the Hill-Mandel condition (4) is always verified. Indeed, this variational statement of the Hill-Mandel condition introduced in [46, 47], see also [45], shows that the admissible kinematic vector field $\mathcal{U}$ is defined by specific boundary conditions whose constraint is to satisfy Eq. (7), in

DOI: 10.1002/nme

which case the the resolution of the micro-scale weak form (10) always ensures Eq. (8), *i.e.* the Hill-Mandel condition (4).

Following the study on the effect of boundary conditions in [25], only the periodic boundary conditions (PBCs) are considered in this work, for which the admissible kinematic vector field $\mathcal{U}$ is defined by

$$\begin{aligned}\mathcal{U}^{\text{PBC}} \quad = \quad & \left\{ \boldsymbol{u}' | \boldsymbol{u}_{\text{m}}(\boldsymbol{x}^+) - \boldsymbol{u}_{\text{m}}(\boldsymbol{x}^-) = (\boldsymbol{u}_{\text{M}} \otimes \nabla_{\text{M}}) \cdot (\boldsymbol{x}^+ - \boldsymbol{x}^-) \,, \right. \\ & \left. \forall \boldsymbol{x}^+ \in \partial\omega^+ \text{ and corresponding } \boldsymbol{x}^- \in \partial\omega^- \right\} \,, \end{aligned} \tag{12}$$

where the parallelepiped SVE faces have been separated in opposite surfaces $\partial\omega^-$ and $\partial\omega^+$. From the definition of the perturbation field (6), one has directly that $\mathcal{U}^{\text{PBC}} \subset \mathcal{U}^{\text{min}}$, and following the previous discussion, the resolution of the weak form (10) always leads to the satisfaction of the Hill-Mandel condition (4). Note that the variational statement does not require the PBCs to constrain directly the symmetry of the surface traction in order to satisfy the Hill-Mandel condition. This symmetry is a consequence of the micro-scale problem resolution as shown by considering arbitrary $\delta\boldsymbol{u}' \in \mathcal{U}^{\text{PBC}}$ in Eq. (9).

2.2.4. Resolution of the constrained micro-scale finite element problem The numerical resolution of the meso-scale BVP relies on the finite elements discretization of the meso-scale volume element ω into ω^e, see Fig. 3(b). Applying the constraint such as the periodic boundary conditions, Eq. (12), on the finite element discretizations of Eq. (10) leads to a set of coupled equations

$$\begin{cases} \mathbf{K}_{\text{m}}\mathbf{u}_{\text{m}} - \mathbf{C}^T\boldsymbol{\lambda} = 0 \,, \text{ and} \\ \mathbf{C}\mathbf{u}_{\text{m}} - \mathbf{S}\mathcal{E}_{\text{M}} = 0 \,, \end{cases} \tag{13}$$

where $\mathbf{K}_{\text{m}}$ is the stiffness matrix of the unconstrained meso-scale volume element, $\mathbf{u}_{\text{m}}$ is the vector of the nodal displacement, $\boldsymbol{\lambda}$ is the vector of the Lagrange multipliers, which enforce the constraints, $\mathcal{E}_{\text{M}}$ represents the macro-scale kinematic variable $\boldsymbol{u}_{\text{M}} \otimes \nabla_{\text{M}}$ written under a vector form, and where $\mathbf{C}$ and $\mathbf{S}$ are the so-called constraints matrix and kinematic matrix, respectively, built from the different constraints.

The stiffness matrix of the meso-scale volume element reads

$$\mathbf{K}_{\text{m}} = \bigwedge_{\omega^e} \int_{\omega^e} (\mathbf{B}^e)^T \mathcal{C}_{\text{m}} \mathbf{B}^e \text{d}V \,, \tag{14}$$

where $\mathcal{C}_{\text{m}}$ is the matrix notation of the micro-scale fourth-order elastic tensor $\mathbb{C}_{\text{m}}$, $\mathbf{B}^e$ is the elementary matrix of the shape functions gradient, and where $\bigwedge_{\omega^e}$ is used to symbolize the assembly process.

In this work, the constraints are the PBCs (12), which have to be applied on a non-periodic mesh. Therefore the polynomial interpolation method [48] is introduced to approximate the PBCs. By considering a pair $i = 1,\ 2,\ 3$ of opposite faces $(\partial\omega_i^-,\ \partial\omega_i^+)$, one can define an interpolation form of

DOI: 10.1002/nme

degree n as

$$\boldsymbol{\varphi}^i(\boldsymbol{x}) = \sum_{k=1}^{n+1} N_k^i(\boldsymbol{x})\, \boldsymbol{a}_k^i \text{ (no sum on } i), \tag{15}$$

where N_k^i with $k = 1, ..., n+1$ are the interpolation shape functions, and $\boldsymbol{a}_k^i$ with $k = 1, ..., n+1$ are first-order tensors of new degrees of freedom corresponding to the interpolation form $\boldsymbol{\varphi}^i$. The PBCs (12) at a boundary position $\boldsymbol{x} \in \partial\omega_i$, thus read

$$\begin{cases} \boldsymbol{u}'\left(\boldsymbol{x}^+; \boldsymbol{a}_1^i, \ldots, \boldsymbol{a}_{n+1}^i\right) & = \boldsymbol{\varphi}^i\left(\boldsymbol{x}^-; \boldsymbol{a}_1^i, \ldots, \boldsymbol{a}_{n+1}^i\right) \ \forall \boldsymbol{x}^+ \in \partial\omega_i^+ \text{, and} \\ \boldsymbol{u}'\left(\boldsymbol{x}^-; \boldsymbol{a}_1^i, \ldots, \boldsymbol{a}_{n+1}^i\right) & = \boldsymbol{\varphi}^i\left(\boldsymbol{x}^-; \boldsymbol{a}_1^i, \ldots, \boldsymbol{a}_{n+1}^i\right) \ \forall \boldsymbol{x}^- \in \partial\omega_i^- \text{.} \end{cases} \tag{16}$$

These equations show that introducing the new degrees of freedom $\boldsymbol{a}_j^i$ with $j = 1, ..., n+1$ allows the fluctuation field to satisfy the PBCs without constraining mesh periodicity. The functions N_k^i depend on the interpolation method considered. Typically 3-dimensional cases are derived using a bilinear patch Coons formulation [48]. Finally, the constraints and kinematic matrices involved in the set of equations (13) are deduced from these functions in Appendix B.

Following the Lagrange multiplier elimination approach summarized in [25, Appendix B], the apparent elasticity tensor can be extracted in the matrix form $\mathcal{C}_{\mathrm{M}}$ as

$$\mathcal{C}_{\mathrm{M}} = \mathbf{D}\tilde{\mathbf{K}}_{\mathrm{m}}^{-1}\left(\mathbf{C}^T - \mathbf{Q}^T\mathbf{K}_{\mathrm{m}}\mathbf{C}^T\left(\mathbf{C}\mathbf{C}^T\right)^{-1}\right)\mathbf{S}\,. \tag{17}$$

In this equation $\mathbf{Q} = \mathbf{I} - \mathbf{C}^T\left(\mathbf{C}\mathbf{C}^T\right)^{-1}\mathbf{C}$, $\tilde{\mathbf{K}}_{\mathrm{m}} = \mathbf{C}^T\mathbf{C} + \mathbf{Q}^T\mathbf{K}_{\mathrm{m}}\mathbf{Q}$, and $\mathbf{D} = \left(\frac{1}{V(\omega)}\bigwedge_{\omega^e}\int_{\omega^e}\mathcal{C}_{\mathrm{m}}\mathbf{B}^e\mathrm{d}V\right)$, see details in [45].

2.3. Apparent elastic properties of SVEs

Applying the homogenization theory described in Section 2.2 on SVE realizations obtained following Section 2.1 allows the apparent elasticity tensors to be extracted in the matrix form $\mathcal{C}_{\mathrm{M}}$. Using the combined pairs of indices as follows: $(\cdot)_{xx} \to (\cdot)_1$, $(\cdot)_{yy} \to (\cdot)_2$, $(\cdot)_{zz} \to (\cdot)_3$, $(\cdot)_{yz} \to (\cdot)_4$, $(\cdot)_{zx} \to (\cdot)_5$ and $(\cdot)_{xy} \to (\cdot)_6$, we convert the obtained homogenized material elastic tensors into their matrix forms, which have a feature as

$$\mathcal{C}_{\mathrm{M}} = \begin{pmatrix} \mathcal{C}_{\mathrm{M11}} & \mathcal{C}_{\mathrm{M12}} & \mathcal{C}_{\mathrm{M13}} & 0.0 & 0.0 & \mathcal{C}_{\mathrm{M16}} \\ & \mathcal{C}_{\mathrm{M22}} & \mathcal{C}_{\mathrm{M23}} & 0.0 & 0.0 & \mathcal{C}_{\mathrm{M26}} \\ & & \mathcal{C}_{\mathrm{M33}} & 0.0 & 0.0 & \mathcal{C}_{\mathrm{M36}} \\ & & & \mathcal{C}_{\mathrm{M44}} & \mathcal{C}_{\mathrm{M45}} & 0.0 \\ & \text{symmetric} & & & \mathcal{C}_{\mathrm{M55}} & 0.0 \\ & & & & & \mathcal{C}_{\mathrm{M66}} \end{pmatrix}, \tag{18}$$

where "$\mathcal{C}_{\mathrm{Mxx}}$" are presented only for non-zero values. The feature of the material tensor (18) results directly from the direct homogenization conducted on the SVEs, in which the fiber are perpendicular to the cross-section. However, as previously stated, the fibers packing is more dense along the ply-thickness (y-direction) than along the ply width (x-direction), meaning that the homogenized

Prepared using nmeauth.cls
DOI: 10.1002/nme

material does not follow a transverse isotropic behavior. As a consequence, there exists a coupling between tension and the xy-shearing, and between the yz-shearing and xz-shearing.

In our previous work [25], the non-zero values $\mathcal{C}_{\mathrm{M16}}$, $\mathcal{C}_{\mathrm{M26}}$, $\mathcal{C}_{\mathrm{M36}}$ and $\mathcal{C}_{\mathrm{M45}}$ were neglected, and an orthogonal anisotropic material model was used to represent the obtained apparent elastic behavior. This assumption is acceptable, because their values are much lower than the diagonal values, *e.g.* for more than 99 % of the realizations of $\mathcal{C}_{\mathrm{M}}$, the absolute values of $\mathcal{C}_{\mathrm{M16}}$, $\mathcal{C}_{\mathrm{M26}}$, and $\mathcal{C}_{\mathrm{M36}}$ were respectively lower than 4.0% of $\mathcal{C}_{\mathrm{M11}}$, 4.0% of $\mathcal{C}_{\mathrm{M22}}$, and 0.2% of $\mathcal{C}_{\mathrm{M33}}$; only $\mathcal{C}_{\mathrm{M45}}$ had an order of magnitude of about 10% of $\mathcal{C}_{\mathrm{M44}}$. In this work, we adopt the same treatment as in [26], where all the non-zero entries are kept in a random vector $\mathcal{V} \in \mathbb{R}^{13}$, to represent the random elastic tensor $\mathcal{C}_{\mathrm{M}}$, and further statistical analyzes will be carried out on this random vector $\mathcal{V}$.

2.4. Statistical analysis on the random apparent material properties

In this section, we study the apparent elastic properties extracted from the stochastic homogenization as described in Section 2.3. First the statistical convergence is studied with respect to the number of realizations. Then, with a view to the comparison with the stochastic M-T model developed in the next section, a PCA is performed on the uncertain apparent material properties.

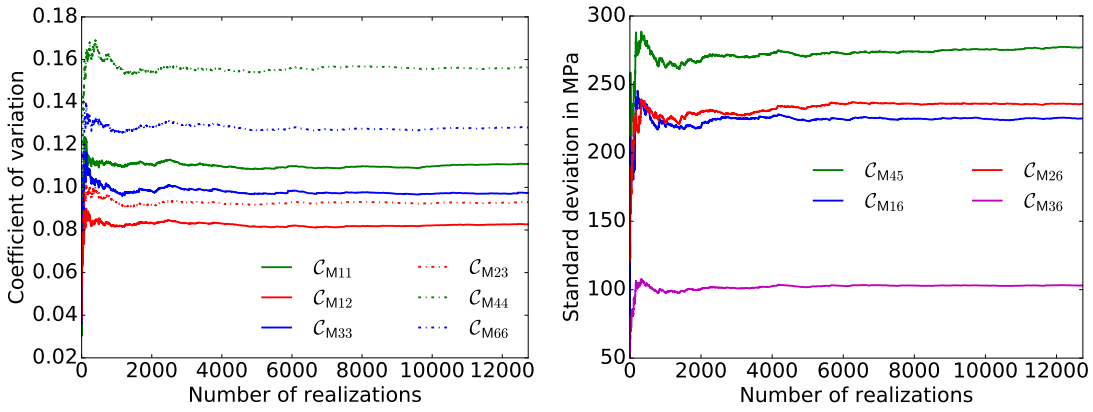

(a) (b)

Figure 4. Statistical convergence of the random apparent elasticity tensor $\mathcal{C}_{\mathrm{M}}$ with the number of realizations.

2.4.1. Statistical convergence of the random apparent elasticity tensors $\mathbb{C}_M$ Totally 12740 realizations of SVEs were used to carry out the computational homogenization. The matrix form (18) of the apparent elastic tensors $\mathcal{C}_{\mathrm{M}}$ is used to study the statistical convergence of the obtained random properties. The estimations of the coefficient of variation of the field $\cdot$, which is defined as the ratio of the standard deviation $\sigma_{\cdot}$ to the standard expectation $\mathbb{E}[\cdot]$, *i.e.* $c_{\mathrm{v}\cdot} = \frac{\sigma_{\cdot}}{\mathbb{E}[\cdot]}$, are plotted in Fig. 4(a) for the entries $\mathcal{C}_{\mathrm{M11}}, \mathcal{C}_{\mathrm{M12}}, \mathcal{C}_{\mathrm{M33}}, \mathcal{C}_{\mathrm{M23}}, \mathcal{C}_{\mathrm{M44}}$, and $\mathcal{C}_{\mathrm{M66}}$. The standard deviations of the other entries that have zero standard expectations, are plotted in Fig. 4(b). The statistical convergence of the random apparent elasticity tensor $\mathcal{C}_{\mathrm{M}}$ is observed in Fig. 4 with an increasing number of realizations. Although the marginal distributions of the random apparent properties have converged after about 3000 realizations, with a view to the construction of a stochastic model involving dependent random variables, we have evaluated more than 12000 realizations in order to be able to construct an accurate empirical copula in Section 5.

DOI: 10.1002/nme

2.4.2. Principal Component Analysis (PCA) applied on the random material properties representation $\mathcal{V}$ The uncertain apparent material properties are represented by a random vector $\mathcal{V}$, who carries the same information as $\mathcal{C}_{\mathrm{M}}$. From the obtained n realizations $\mathbf{v}_i$ $(i = 1, ..., n)$, the mean vector $\boldsymbol{\mu}_{\mathcal{V}}$ of $\mathcal{V}$ can be estimated by

$$\boldsymbol{\mu}_{\mathcal{V}} = \frac{1}{n}\sum_{i=1}^{n} \mathbf{v}_i \,, \tag{19}$$

and the variance $\sigma_{\mathcal{V},r}$ of each of its entry r $(r = 1, ..., 13)$ results from

$$\sigma^2_{\mathcal{V},r} = \frac{1}{n-1}\sum_{i=1}^{n} (\mathrm{v}_{i,r} - \mu_{\mathcal{V},r})^2 \,. \tag{20}$$

Before carrying out the PCA, a normalization is performed on $\mathbf{v}_i$ $(i = 1, ..., n)$ by

$$\tilde{\mathrm{v}}_{i,r} = \frac{(\mathrm{v}_{i,r} - \mu_{\mathcal{V},r})}{\sigma_{\mathcal{V},r}} \,, r = 1, ..., 13 \,. \tag{21}$$

We define the data matrix $\tilde{\boldsymbol{V}} = \{\tilde{\mathbf{v}}_1, \tilde{\mathbf{v}}_2, ..., \tilde{\mathbf{v}}_n\} \in \mathbb{R}^{13\times n}$, and the matrix $\boldsymbol{W} = \tilde{\boldsymbol{V}}\tilde{\boldsymbol{V}}^{\mathrm{T}} \in \mathbb{R}^{13\times 13}$. The 13 eigenvalues of $\boldsymbol{W}$ are denoted in a descending order as $\Lambda_1 \geq \Lambda_2 \geq ... \geq \Lambda_{13}$, and their corresponding eigenvectors as $\underline{\boldsymbol{u}}_1$, $\underline{\boldsymbol{u}}_2$, ..., $\underline{\boldsymbol{u}}_{13}$. The criterion

$$1.0 - \frac{\sum_{i=1}^{p} \Lambda_i}{\sum_{i=1}^{13} \Lambda_i} \leq \delta \quad \text{with} \quad p \leq 13 \,, \tag{22}$$

where δ, a small value close to zero, controls the accuracy of the order reduction –*e.g.* if we set $\delta = 0.0$, this means that either we keep the original dimension $p = 13$, or $\boldsymbol{W}$ has at least one zero eigen value and $p < 13$. Finally we define

$$\boldsymbol{U} = \left[\underline{\boldsymbol{u}}_1, \underline{\boldsymbol{u}}_2, ..., \underline{\boldsymbol{u}}_p\right]_{13\times p} \,, \tag{23}$$

and the dimensionaly reduced data matrix

$$\mathbf{X}_{p\times n} = \boldsymbol{U}^{\mathrm{T}}\tilde{\boldsymbol{V}} \,. \tag{24}$$

A random vector generator can be constructed based on the dimensionaly reduced data matrix $\mathbf{X}$, *e.g.* using the copula method [42]. From the generated random vector $\mathbf{x}$, the random vector $\tilde{\mathbf{v}}$, which has the original dimension of 13, can be estimated by $\tilde{\mathbf{v}} = \boldsymbol{U}\mathbf{x}$. By passing the inverse process of Eq. (21), the desired realizations $\mathbf{v}$ of the random vector $\mathcal{V}$ are recovered.

Table I. Reduced order p and corresponding accuracy measure δ for the random vector $\mathcal{V}$

p	3	4	5	6	7	8	9
δ	0.0648	0.0345	0.0137	0.0071	0.0035	0.0018	0.0006

A PCA analysis is performed on the 12740 realizations of $\mathcal{V}$. The values of the reduced order p and their corresponding accuracy δ, Eq. (22), are presented in Table I. Table I shows that $p \geq 5$ is

DOI: 10.1002/nme

required during the order reduction on the random vector $\mathcal{V}$ in order to keep a reasonable accuracy, *i.e.* better than 98%. Finally the random vector $\mathcal{V} \in \mathbb{R}^{13}$ can be represented by a lower order random vector which is denoted as $\mathcal{X} \in \mathbb{R}^p$ with $5 \leq p < 13$.

In this section, it was shown that an order reduction on random apparent elastic properties of SVEs could be carried out by a series of simple mathematical operations. PCA analysis is a widely used statistic procedure for the purpose of random vector dimensional reduction and random vector generation. However, for our specific problem of SVEs, some basic micro-structure information, such as fiber volume fraction, shape of fibers, *etc.* are never used in PCA. In fact, if we use the apparent elastic properties of SVEs in a direct way, there is no access to get even qualitative information of the local phases (fiber, matrix) because these apparent elastic properties are totally disconnected with their associated micro-structures. As a result, further nonlinear analyzes, in particular history-dependent ones, will become rather complex, *e.g.* plasticity and/or damage and/or failure descriptions need to be stated in an anisotropic way, which means a lot of parameters will be required to model the nonlinear behavior of the material. With the view of having a simple stochastic description for the nonlinear behavior of composites, a micro-mechanical analysis, which also has the effect of order reduction, is introduced in the next Section.

3. MICRO-MECHANICS BASED ORDER REDUCTION

In this section, the main equations of the mean-field homogenization (MFH) method for two-phase composites are summarized in the context of linear elasticity. In particularly, we consider the Mori-Tanaka (M-T) assumption. With a view to performing a micro-structure related order reduction on the random apparent elastic properties of the SVEs, the M-T model is compared to the computational homogenization. Using as input the elastic properties resulting from the stochastic computational homogenization, an inverse stochastic identification of the M-T model is then stated. Eventually the inverse identification results are statistically analyzed.

3.1. MFH method and Mori-Tanaka model for two-phase linear elastic composites

In a multiscale procedure as illustrated in Fig. 1, a MFH method defines the relation between the meso-strain tensor $\boldsymbol{\varepsilon}_{\mathrm{M}}$ and meso-stress tensor $\boldsymbol{\sigma}_{\mathrm{M}}$ into a relation between average strain tensor $<\boldsymbol{\varepsilon}_{\mathrm{m}}>$ and stress tensor $<\boldsymbol{\sigma}_{\mathrm{m}}>$ over the volume element ω. We use the terminology "meso-scale" to indicate the homogenized value on a volume element in order to stay consistent with the notation of Section 2. Considering a two-phase isothermal linear elastic composite material, with uniform constitutive material stiffness tensors $\mathbb{C}_0$ for the matrix and $\mathbb{C}_{\mathrm{I}}$ for the inclusions, and with the respective volume fractions $v_0 + v_{\mathrm{I}} = 1$ (subscript 0 refers to the matrix and I to the inclusions), the homogenized strain and stress tensors can be written in terms of the volume-averaged values over the matrix subdomain ω_0 and the inclusions subdomain ω_{I} as

$$\begin{aligned} \boldsymbol{\varepsilon}_{\mathrm{M}} &= v_0 <\boldsymbol{\varepsilon}_{\mathrm{m}}>_{\omega_0} + v_{\mathrm{I}} <\boldsymbol{\varepsilon}_{\mathrm{m}}>_{\omega_{\mathrm{I}}} \quad \text{and} \\ \boldsymbol{\sigma}_{\mathrm{M}} &= v_0 <\boldsymbol{\sigma}_{\mathrm{m}}>_{\omega_0} + v_{\mathrm{I}} <\boldsymbol{\sigma}_{\mathrm{m}}>_{\omega_{\mathrm{I}}} . \end{aligned} \tag{25}$$

Prepared using nmeauth.cls
DOI: 10.1002/nme

In order to solve the relation between $\boldsymbol{\varepsilon}_{\mathrm{M}}$ and stresses $\boldsymbol{\sigma}_{\mathrm{M}}$, the system of Eqs. (25) is completed by an equation describing the relation between the strain averages per phase through a strain concentration tensor $\mathbb{B}^{\epsilon}$:

$$< \boldsymbol{\varepsilon}_{\mathrm{m}} >_{\omega_{\mathrm{I}}} = \mathbb{B}^{\epsilon} :< \boldsymbol{\varepsilon}_{\mathrm{m}} >_{\omega_0} \ . \tag{26}$$

Different assumptions on the micro-mechanics have been made in different MFH models to approximate the solution of $\mathbb{B}^{\epsilon}$, see *e.g.* [49, 33]. For the Mori-Tanaka (M-T) model, the strain concentration tensor is given by

$$\hat{\mathbb{B}}^{\epsilon} = \{\mathbb{I} + \mathbb{S} : [(\mathbb{C}_0)^{-1} : \mathbb{C}_{\mathrm{I}} - \mathbb{I}]\}^{-1} , \tag{27}$$

where $\hat{\mathbb{B}}^{\epsilon}$ is used to indicate the approximated $\mathbb{B}^{\epsilon}$, the Eshelby tensor $\mathbb{S}(\mathrm{I}, \mathbb{C}_0)$ depends on the geometry of inclusions (I) and on $\mathbb{C}_0$ [50], and $\mathbb{I}$ is the fourth-order symmetric identity tensor given in Appendix A.

Therefore, using Eqs. (25-27), the meso-scale homogenized material behavior is written under the form

$$\hat{\boldsymbol{\sigma}}_{\mathrm{M}} = \hat{\mathbb{C}}_{\mathrm{M}} : \boldsymbol{\varepsilon}_{\mathrm{M}} , \text{ with } \hat{\mathbb{C}}_{\mathrm{M}} = [v_{\mathrm{I}}\mathbb{C}_{\mathrm{I}} : \hat{\mathbb{B}}^{\epsilon} + v_0\mathbb{C}_0] : [v_{\mathrm{I}}\hat{\mathbb{B}}^{\epsilon} + v_0\mathbb{I}]^{-1} , \tag{28}$$

where $\hat{\boldsymbol{\sigma}}_{\mathrm{M}}$ refers to the approximated values of $\boldsymbol{\sigma}_{\mathrm{M}}$, and $\hat{\mathbb{C}}_{\mathrm{M}}$ is the meso-scale homogenized material tensor resulting from the MFH model. Equation (28) shows that the apparent meso-scale elasticity tensor $\hat{\mathbb{C}}_{\mathrm{M}}$ of composites can be computed from the elasticity tensors of the matrix, $\mathbb{C}_0$, and of the fiber $\mathbb{C}_{\mathrm{I}}$, from the volume fraction of fibers v_{I}, and from the geometrical information of fibers (I).

3.2. Comparison between the mean-field homogenization and the computational homogenization

The MFH and the computational homogenization methods have identical definitions on the homogenized meso-scale strain tensor $\boldsymbol{\varepsilon}_{\mathrm{M}}$ and stress tensor $\boldsymbol{\sigma}_{\mathrm{M}}$, which are respectively the volume averaged values of their micro-scale counterparts $\boldsymbol{\varepsilon}_{\mathrm{m}}$ and $\boldsymbol{\sigma}_{\mathrm{m}}$, see Eqs. (5) and (25). In the context of linear elasticity, the meso-scale homogenized material behaviors are stated as

$$\boldsymbol{\sigma}_{\mathrm{M}} = \mathbb{C}_{\mathrm{M}} : \boldsymbol{\varepsilon}_{\mathrm{M}} \text{ and } \hat{\boldsymbol{\sigma}}_{\mathrm{M}} = \hat{\mathbb{C}}_{\mathrm{M}} : \boldsymbol{\varepsilon}_{\mathrm{M}} , \tag{29}$$

for computational homogenization and MFH, respectively. Besides, in linear elastic region, the elastic energy density on the meso-scale volume element ω is expressed as

$$\phi \ = \ \frac{1}{2} < \boldsymbol{\sigma}_{\mathrm{m}} : \boldsymbol{\varepsilon}_{\mathrm{m}} >_{\omega} , \tag{30}$$

which is rewritten as

$$\begin{aligned} \phi &= \frac{1}{2}\boldsymbol{\sigma}_{\mathrm{M}} : \boldsymbol{\varepsilon}_{\mathrm{M}} = \frac{1}{2}\mathbb{C}_{\mathrm{M}} :: (\boldsymbol{\varepsilon}_{\mathrm{M}} \otimes \boldsymbol{\varepsilon}_{\mathrm{M}}) \text{ and} \\ \hat{\phi} &= \frac{1}{2}\hat{\boldsymbol{\sigma}}_{\mathrm{M}} : \boldsymbol{\varepsilon}_{\mathrm{M}} = \frac{1}{2}\hat{\mathbb{C}}_{\mathrm{M}} :: (\boldsymbol{\varepsilon}_{\mathrm{M}} \otimes \boldsymbol{\varepsilon}_{\mathrm{M}}) , \end{aligned} \tag{31}$$

for computational homogenization and MFH, respectively.

Prepared using nmeauth.cls
DOI: 10.1002/nme

In general, for the same meso-scale strain tensor $\boldsymbol{\varepsilon}_{\mathrm{M}}$, $\hat{\boldsymbol{\sigma}}_{\mathrm{M}} \neq \boldsymbol{\sigma}_{\mathrm{M}}$, $\hat{\mathbb{C}}_{\mathrm{M}} \neq \mathbb{C}_{\mathrm{M}}$, and $\hat{\phi} \neq \phi$. This is particularly true in the context of Stochastic Volume Elements, for which computational homogenization does not lead to unique homogenized value.

On the one hand, assuming the size of the meso-scale volume element is large enough, statistical representativity is ensured and the meso-scale volume element is called Representative Volume Element (RVE). In that case, the meso-scale elasticity tensor $\mathbb{C}_{\mathrm{M}}$ obtained by computational homogenization is unique. It is however not always equal to $\hat{\mathbb{C}}_{\mathrm{M}}$, since the latter is derived from an approximated mean (volume averaged) strain concentration tensor and micro-mechanics assumptions, such as the M-T model. Nevertheless in the case of (possibly transversely anisotropic) inclusions embedded in an isotropic matrix, the M-T model has been shown to be able to provide good predictions for low to moderate volume fractions of inclusions [51], *i.e.* $\hat{\mathbb{C}}_{\mathrm{M}} = \mathbb{C}_{\mathrm{M}}$.

On the other hand, when considering Stochastic Volume Elements (SVEs), the apparent meso-scale elasticity tensor $\mathbb{C}_{\mathrm{M}}$ extracted from full-field finite element resolutions is not unique. It depends on the micro-structure realization, characterized by a given arrangement of inclusions, and on the defined boundary conditions. Since in this work, we are dealing with volume elements of limited size, SVEs, the inclusion arrangement always affects the homogenized material tensor, $\mathbb{C}_{\mathrm{M}}$, obtained by computational homogenization. However, the apparent meso-scale elasticity tensor $\hat{\mathbb{C}}_{\mathrm{M}}$ is *a priori* unique since the MFH method does not require defining special boundary conditions, and since there is no definition of a meso-scale length scale such as the length of the meso-scale volume element ω. In fact, for volume elements of inclusion reinforced matrix materials with constant inclusion volume fraction v_{I}, and inclusion orientation, the obtained $\hat{\mathbb{C}}_{\mathrm{M}}$ is unique.

In the next sections we will thus consider the input of the MFH as random variables in order to recover the uncertain behavior observed with computation homogenization in Section 2.3.

3.3. Inverse stochastic identification of the M-T model

The purpose of this section is to reproduce with mean-field homogenization, in particular with the Mori-Tanaka model, the uncertainties observed in the meso-scale apparent elasticity tensor $\mathbb{C}_{\mathrm{M}}$ extracted by computational homogenization on the SVE realizations.

The meso-scale material tensor $\hat{\mathbb{C}}_{\mathrm{M}}$ is evaluated by the M-T method by combining Eqs. (27-28), and it depends on the elasticity tensors of the matrix $\mathbb{C}_0$, and of the fiber $\mathbb{C}_{\mathrm{I}}$, the volume fraction of fibers v_{I}, and on the geometrical information of the inclusions (I). The inverse problem thus reads for each realization

$$\hat{\mathbb{C}}_{\mathrm{M}}(\hat{\mathbf{I}}, \hat{\mathbb{C}}_0, \hat{\mathbb{C}}_{\mathrm{I}}, \hat{v}_{\mathrm{I}}, \boldsymbol{\theta}) \approx \mathbb{C}_{\mathrm{M}}\,, \tag{32}$$

where a rotation angles vector $\boldsymbol{\theta}$ has been included in order for the elasticity tensor of inclusion, $\mathbb{C}_{\mathrm{I}}$, and the Eshelby's tensor, $\mathbb{S}$, to be expressed in the local coordinates of the inclusion. In Eq. (32), we have used the "$\hat{\cdot}$" notation to differentiate the effective values of the fields that satisfy the approximation (32) from the original ones used during the computational homogenization in Section 2.3.

When considering an isotropic matrix material, *i.e.* $\hat{\mathbb{C}}_0$ is isotropic, the anisotropy of $\hat{\mathbb{C}}_{\mathrm{M}}$ can result from the anisotropy of $\hat{\mathbb{C}}_{\mathrm{I}}$ and/or from the non spherical shape of inclusion (I), which will lead to an orthogonal anisotropic homogenized tensor $\hat{\mathbb{C}}_{\mathrm{M}}$. Therefore, it is possible to reproduce an

DOI: 10.1002/nme

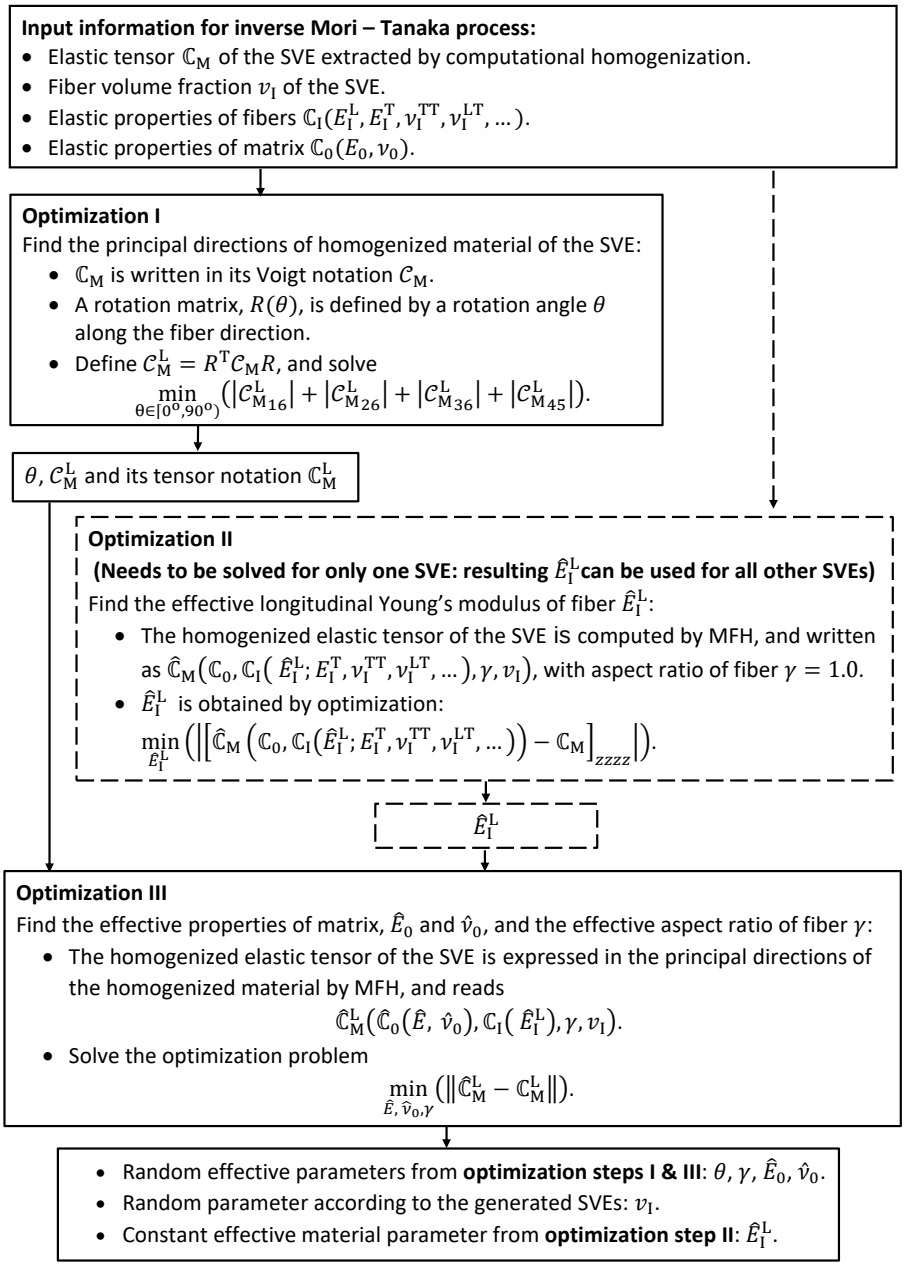

Figure 5. Flowchart of the inverse identification of the M-T model for one SVE.

anisotropic apparent elasticity tensor $\mathbb{C}_M$ with $\hat{\mathbb{C}}_M$. The inverse resolution is summarized in Fig. 5, and the different steps are detailed in the following paragraphs.

3.3.1. The anisotropy of $\mathbb{C}_M$ and $\hat{\mathbb{C}}_M$ Let the three principal directions of the homogenized material be denoted by x', y' and z', with the material principal direction z' identical to the z-direction of the SVEs, and which refers to the longitudinal direction "L" along the fiber direction. The feature of the homogenized elastic tensor $\mathbb{C}_M$ in its matrix form $\mathcal{C}_M$, Eq. (18), indicates two kinds of possible material anisotropy:

DOI: 10.1002/nme

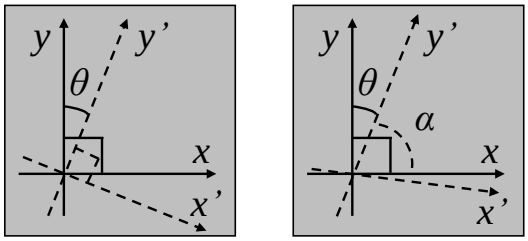

(a) Orthogonal anisotropy (b) Monoclinic anisotropy

Figure 6. Anisotropic material system, with $x' - y'$ referring to the material coordinates and $x - y$ to the SVE coordinates.

- Orthogonal anisotropy, see Fig. 6(a), for which the principal material directions x' and y' are orthogonal to each other, and a rotation angle θ has to be defined between the material coordinates $x' - y'$ and the SVE coordinates $x - y$.
- Monoclinic anisotropy, see Fig. 6(b), for which the principal material directions x' and y' are not orthogonal to each other but separated by an angle $\alpha \neq 90^{\text{o}}$, in which case the rotation angle θ between material coordinates $x' - y'$ and SVE coordinates $x - y$ refers to the y-direction.

The rotation angle θ defines a 6×6-rotation matrix $\boldsymbol{R}(\theta)$, such that

$$\mathcal{C}_{\text{M}}^{\text{L}} = \boldsymbol{R}^{\text{T}}(\theta)\mathcal{C}_{\text{M}}\boldsymbol{R}(\theta)\,, \tag{33}$$

where $\mathcal{C}_{\text{M}}^{\text{L}}$ is the matrix form of a homogenized elasticity tensor expressed in its local material coordinates. This rotation angle θ results from an optimization problem, which reads

$$\min_{\theta\in[0^{\text{o}},90^{\text{o}})} (|\mathcal{C}_{\text{M16}}^{\text{L}}| + |\mathcal{C}_{\text{M26}}^{\text{L}}| + |\mathcal{C}_{\text{M36}}^{\text{L}}| + |\mathcal{C}_{\text{M45}}^{\text{L}}|)\,, \tag{34}$$

where $\mathcal{C}_{\text{M16}}^{\text{L}}$, $\mathcal{C}_{\text{M26}}^{\text{L}}$, $\mathcal{C}_{\text{M36}}^{\text{L}}$ and $\mathcal{C}_{\text{M45}}^{\text{L}}$ are four entries of $\mathcal{C}_{\text{M}}^{\text{L}}$, see Eq. (18). The optimum value of Eq. (34) reaches zero when the homogenized material properties are orthogonal anisotropic.

In this paper, considering more than 12000 realizations of $\mathcal{C}_{\text{M}}$ corresponding to more than 12000 SVE realizations of size $25 \times 25 \times 1\mu\text{m}^3$, Eq. (34) always reaches 0 or a value which is several orders of magnitude lower than the diagonal entries $\mathcal{C}_{\text{M}}^{\text{L}}$. This means that either $\alpha = 90^{\text{o}}$ or $\alpha \approx 90^{0}$, see Fig. 6(b), and that the homogenized behavior can be approximated by an orthogonal anisotropic material.

3.3.2. Introduction of the inverse identification Since each realization of $\mathbb{C}_{\text{M}}$ is associated to a SVE realization, which is characterized by a given volume fraction of inclusions v_{I}, a $\mathbb{C}_{\text{M}}$ is associated to a volume fraction v_{I}. Moreover, following the argumentation in Section 3.3.1, the rotation angles vector $\boldsymbol{\theta}$ can be reduced to an angle θ, which can be determined by solving the optimization problem (34). Hence, with given values of v_{I} and θ the general inverse problem (32) is simplified for UD composite materials as

$$\hat{\mathbb{C}}_{\text{M}}(\hat{\text{I}}, \hat{\mathbb{C}}_0, \hat{\mathbb{C}}_{\text{I}}; v_{\text{I}}, \theta) \approx \mathbb{C}_{\text{M}}\,, \tag{35}$$

DOI: 10.1002/nme

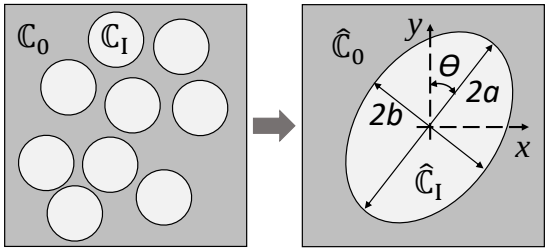

Figure 7. Illustration of the inverse identification of mean-field homogenization model for UD composite materials.

where $\hat{\mathbb{C}}_0$ and $\hat{\mathbb{C}}_\mathrm{I}$ are the effective elasticity tensors of matrix and inclusion, respectively. The effective inclusion geometry $\hat{\mathrm{I}}$ together with θ reflect the distribution of unidirectional fibers in the matrix. Figure 7 illustrates the simplified inverse problem for UD composites.

In fact, defining *ad hoc* elasticity tensors of the phases is really common in MFH, especially for nonlinear analyzes in which a Linear Comparison Composite (LCC) is usually defined depending on the adopted scheme. In particular, variational schemes of MFH define the effective elastic tensors of phases by minimizing the difference between the energy of the homogenized system and that of the real system. In our problem, $\hat{\mathbb{C}}_\mathrm{M} \approx \mathbb{C}_\mathrm{M}$ is equivalent to state that $\hat{\phi} \approx \phi$ in Eq. (31), *cf.* the discussion in Section 3.2.

Using the value of θ obtained from Eq. (34), we can write $\hat{\mathbb{C}}_\mathrm{M}$ and $\mathbb{C}_\mathrm{M}$ in their local material principal coordinates, and the effective elasticity tensors of the matrix and inclusion phases can be identified through a simplified optimization problem, which reads

$$\min_{\hat{\mathrm{I}},\hat{\mathbb{C}}_0,\hat{\mathbb{C}}_\mathrm{I}} \|\hat{\mathbb{C}}^\mathrm{L}_\mathrm{M}(\hat{\mathrm{I}},\hat{\mathbb{C}}_0,\hat{\mathbb{C}}_\mathrm{I};v_\mathrm{I}) - \mathbb{C}^\mathrm{L}_\mathrm{M}\|\,, \tag{36}$$

where $\|\cdot\|$ refers to the Frobenius norm. Note that, for each realization, v_I is a known value associated to the SVE from which $\mathbb{C}^\mathrm{L}_\mathrm{M}$ is computed. The arguments of this optimization problem (36) can be further simplified with the following specializations:

- In the real material system whose micro-structure was statistically studied in [25], the fibers have the shape of circular cylinders and are randomly distributed in the matrix. In the effective material system, we use isotropically distributed right elliptic cylinders to imitate the real system, see Fig 7. Therefore, the shape of the effective inclusions is defined by the semi-axes a and b of their elliptic cross section, and in order to characterize $\hat{\mathrm{I}}$, only one parameter is needed and is defined by $\gamma = b/a$. The effective inclusions shape is thus denoted by $\hat{\mathrm{I}}(\gamma)$.
- For the matrix phase, we assume that the effective matrix material follows an isotropic behavior so that $\hat{\mathbb{C}}_0$ is defined by the effective Young's modulus $\hat{E}_0$ and effective Poisson ratio $\hat{\nu}_0$. The effective matrix elasticity tensor is denoted by $\hat{\mathbb{C}}_0(\hat{E}_0,\hat{\nu}_0)$.
- For UD-fiber reinforced composites, the material response is dominated by the behavior of the matrix phase when transversely loaded and by that of the fiber phase when longitudinally loaded. Therefore, in order to define the effective transverse isotropic elasticity tensor of the fiber $\hat{\mathbb{C}}_\mathrm{I}$, we keep the original transverse-related material properties, *i.e.* E^T_I, $\nu^\mathrm{TT}_\mathrm{I}$, $\nu^\mathrm{LT}_\mathrm{I}$, G^TT_I and G^LT_I, see Section 2.3, are kept as such. However, since using M-T model on UD-fiber reinforced composites leads to the result of Voigt assumption for the response in the

DOI: 10.1002/nme

longitudinal direction, which is an upper bound for the homogenized property, in order to obtain an accurate homogenized response with the M-T model, a reduced longitudinal Young's modulus $\hat{E}_{\mathrm{I}}^{\mathrm{L}}$ is used instead of its original value. The effective inclusion elasticity tensor is thus denoted by $\hat{\mathbb{C}}_{\mathrm{I}}(\hat{E}_{\mathrm{I}}^{\mathrm{L}})$. The reduced $\hat{E}_{\mathrm{I}}^{\mathrm{L}}$ can be obtained through a simple pre-step, which reads,

$$\min_{\hat{E}_{\mathrm{I}}^{\mathrm{L}}} \left| \left[\hat{\mathbb{C}}_{\mathrm{M}}(\mathrm{I}, \mathbb{C}_0, \hat{\mathbb{C}}_{\mathrm{I}}(\hat{E}_{\mathrm{I}}^{\mathrm{L}}); v_{\mathrm{I}}) - \mathbb{C}_{\mathrm{M}} \right]_{zzzz} \right| , \tag{37}$$

where $[\cdot]_{zzzz}$ indexes the entry of a fourth-order tensor along the fibers direction. In Eq. (37), $\hat{E}_{\mathrm{I}}^{\mathrm{L}}$ is the only argument, all the other material parameters take their original value. Solving the optimization problem (37) with more than 12000 realizations of $\mathbb{C}_{\mathrm{M}}$ shows that the resulting $\hat{E}_{\mathrm{I}}^{\mathrm{L}}$ is an almost constant value for all the realizations of $\mathbb{C}_{\mathrm{M}}$, as it will be discussed in the next Section.

According to these previous analyzes, the optimization problem (36) simplifies into

$$\min_{\hat{E}_0, \hat{\nu}_0, \gamma} \| \hat{\mathbb{C}}_{\mathrm{M}}^{\mathrm{L}}(\hat{E}_0, \hat{\nu}_0, \gamma; v_{\mathrm{I}}, \hat{E}_{\mathrm{I}}^{\mathrm{L}}) - \mathbb{C}_{\mathrm{M}}^{\mathrm{L}} \| . \tag{38}$$

The Eshelby tensor $\mathbb{S}(\hat{\mathrm{I}}, \hat{\mathbb{C}}_0)$ for cylindrical inclusions required for this optimization process is detailed in Appendix C.

3.4. The stochastic M-T model

Based on the 12740 realizations of $\mathbb{C}_{\mathrm{M}}$ obtained in Section 2.3, the inverse stochastic identification of the M-T model, which is expressed by a series of optimization problems Eqs. (34), (37) and (38) as developed in Section 3.3, see also Fig. 5, is performed in order to extract the geometrical parameters θ and γ, and the effective properties $\hat{E}_{\mathrm{I}}^{\mathrm{L}}$, $\hat{E}_0$ and $\hat{\nu}_0$. Practically, these optimization steps are performed using the SciPy library of Python.

3.4.1. The reduced longitudinal Young's modulus of fiber $\hat{E}_I^L$ By solving the optimization problem stated by Eq. (37), the obtained $\hat{E}_{\mathrm{I}}^{\mathrm{L}}$ realizations turn out to be almost constant for all the realizations of $\mathbb{C}_{\mathrm{M}}$: a value $\hat{E}_{\mathrm{I}}^{\mathrm{L}} = 222.1$ GPa is found and has to be compared with the original of value 230.0 GPa. This $\hat{E}_{\mathrm{I}}^{\mathrm{L}} = 222.1$ GPa value is thus used as a known parameter in the optimization problem stated by Eq. (38).

3.4.2. Random geometrical and material parameters of the M-T model The random apparent elastic properties of the SVE realizations, which were represented by a random vector $\mathcal{V} \in \mathbb{R}^{13}$ in Section 2.3, are now represented by a new random vector $\mathcal{V}_{\text{M-T}} = [v_{\mathrm{I}}, \theta, \gamma, \hat{E}_0, \hat{\nu}_0]^{\mathrm{T}} \in \mathbb{R}^5$ obtained by the resolution of the inverse identification of the M-T model. This random vector $\mathcal{V}_{\text{M-T}}$ gathers the random material properties, $\hat{E}_0$ and $\hat{\nu}_0$, and the random micro-structural information v_{I}, θ, and γ[†].

[†]In the optimization problem (34), θ is constrained in $[0^{\mathrm{o}}, 90^{\mathrm{o}})$ because of the periodicity of its objective function in terms of θ. For a given value of θ, the optimization process (38) identifies the aspect ratio, $\gamma = b/a$, of the elliptic cross section of the fictitious fibers, Fig. 7. Depending on the real fibers distribution of each SVE, the resulting value of γ could

DOI: 10.1002/nme

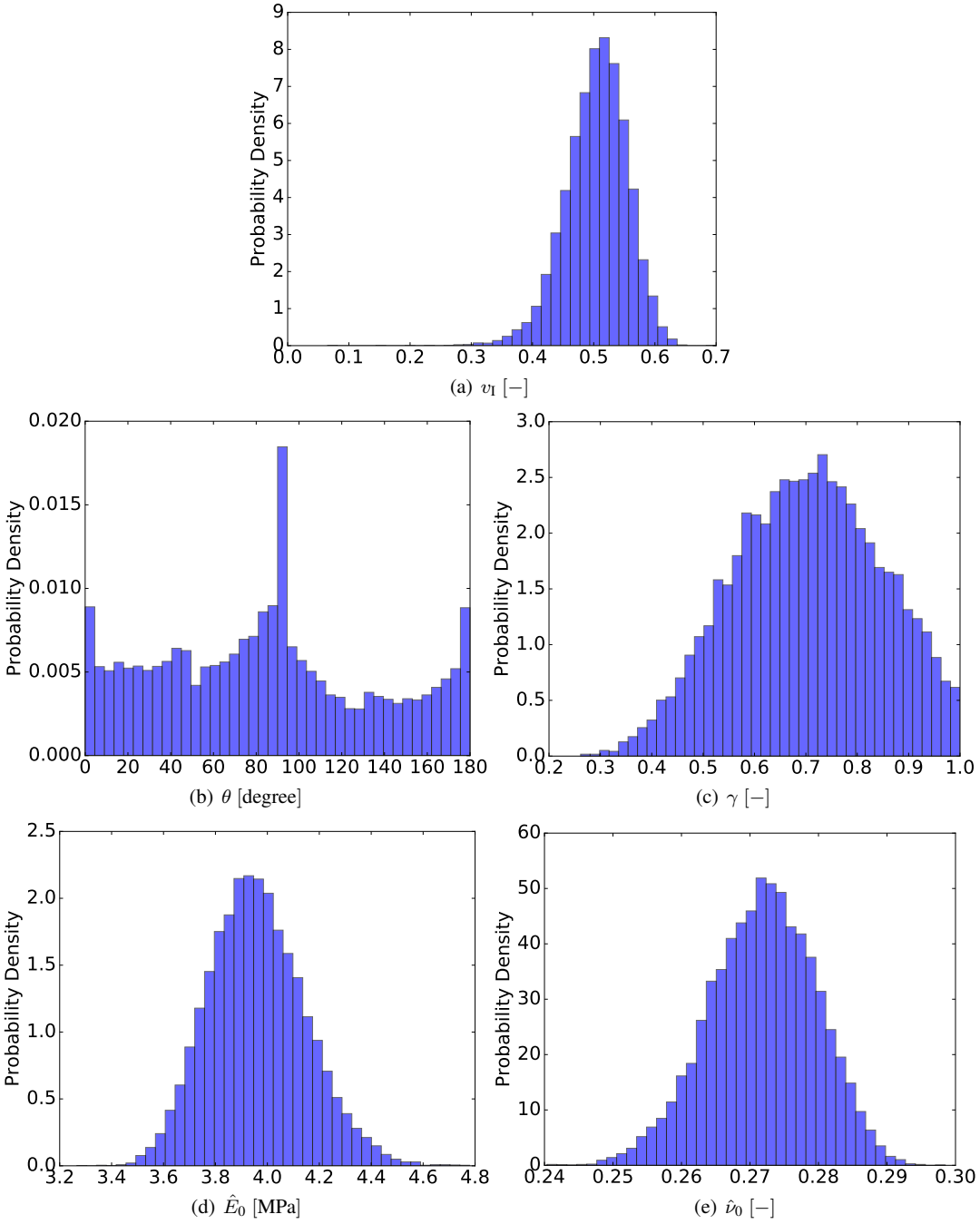

Figure 8. The histograms of the random micro-structure (a-c) and material (d-e) parameters of the stochastic M-T model.

be

$$\begin{cases} \gamma \leq 1.0\,, & \text{if } b \leq a \quad \text{or} \\ \gamma > 1.0\,, & \text{if } b > a\,. \end{cases} \tag{39}$$

In order to limit the range of γ, *e.g.* $\gamma \in (0, 1]$, a simple operation is performed according to the rotational symmetry of an elliptical cylinder: for the case of $\gamma > 1.0$, the values of a and b are exchanged and θ is set to $\theta + 90^{\mathrm{o}}$. Therefore, for

Prepared using nmeauth.cls
DOI: 10.1002/nme

The histograms of the entries of $\mathcal{V}_{\text{M-T}}$ are given in Fig. 8. Since the values of v_{I} are directly extracted from the SVE realizations, the related histogram, Fig. 8(a), is defined by the micro-structure generator developed in [25]. The random variables θ and γ partly reflect the micro-structure information of the SVEs and their histograms, see Figs. 8(b) and 8(c), are also related to the micro-structure generator to a certain degree. Indeed, it was shown in [25] that the fibers are seldom isotropically distributed in the matrix phase, leading to an anisotropic behavior in the two transverse directions. The effective matrix material properties, *i.e.* the Young's modulus $\hat{E}_0$ and the Poisson ratio $\hat{\nu}_0$, are close to their original values, respectively $E_0 = 3.2$GPa and $\nu_0 = 0.3$, see Figs. 8(d) and 8(e). However, it can be seen that $\hat{E}_0 > E_0$ and $\hat{\nu}_0 < \nu_0$.

Figure 8 shows that the distributions of all these random variables are non-Gaussian. In order not to assume a particular distribution type, the empirical copula method will be used in Section 5 as a stochastic model, which requires first to assess their statistical dependence. Since their distributions are non-Gaussian, the statistical dependence of the random variables must be assessed by their distance correlations [52]. The obtained distance correlation matrix of the five random variables reads

$$\mathbf{dCor} = \begin{array}{c} \\ v_{\text{I}} \\ \theta \\ \gamma \\ \hat{E}_0 \\ \hat{\nu}_0 \end{array} \begin{array}{c} \begin{array}{ccccc} v_{\text{I}} & \theta & \gamma & \hat{E}_0 & \hat{\nu}_0 \end{array} \\ \begin{pmatrix} 1.0 & 0.015 & 0.114 & 0.523 & 0.499 \\ & 1.0 & 0.092 & 0.016 & 0.014 \\ & & 1.0 & 0.080 & 0.076 \\ & \text{symmetric} & & 1.0 & 0.661 \\ & & & & 1.0 \end{pmatrix} \end{array}. \tag{41}$$

The dependency between any two of these random variables is characterized by the corresponding entry in this distance correlation matrix (41), which indicates that they need to be treated as statistical dependent random variables.

We need to remind that using the random vector $\mathcal{V}_{\text{M-T}}$ alone is not enough to reproduce the random apparent properties of SVEs: the constant elastic tensor of fibers, $\hat{\mathbb{C}}_{\text{I}}(\hat{E}_{\text{I}}^{\text{L}})$, is still needed.

3.4.3. Discussion on the order reduction The classical statistical order reduction procedure based on the PCA has been introduced in Section 2.4.2, where it has been applied on $\mathcal{V}$, the vector representation of the 12740 realizations of $\mathbb{C}_{\text{M}}$. It has been concluded that at least 5 random variables (*i.e.* 5 dimensions) are required in order to describe the uncertainties of the homogenized meso-scale material properties.

Table II. Reduced order p and corresponding accuracy measure δ for the random vector $\mathcal{V}_{\text{M-T}}$

p	3	4	5
δ	0.1539	0.0550	0.00

the two geometrical random variables, we have

$$\theta \in [0^{\text{o}}, 180^{\text{o}}) \text{ and } \gamma \in (0, 1.0]\,. \tag{40}$$

DOI: 10.1002/nme

The stochastic M-T model uses the random vector $\mathcal{V}_{\text{M-T}} = [v_{\text{I}}, \theta, \gamma, \hat{E}_0, \hat{\nu}_0]^{\text{T}}$ to compute the uncertain homogenized meso-scale material properties. A PCA is also performed on $\mathcal{V}_{\text{M-T}}$, which also includes 12740 realizations resulting from the inverse stochastic identification of the M-T model, to study the possibility of further order reduction. The results of the PCA and order reduction on $\mathcal{V}_{\text{M-T}}$ are given in Table II, see Eq. (22). The results in Table II indicate that the random vector $\mathcal{V}_{\text{M-T}}$ indeed includes the variations in 5 dimensions. Therefore, the order of $\mathcal{V}_{\text{M-T}}$ cannot be reduced anymore from the aspect of accuracy in order to preserve enough information of the uncertainties.

4. VERIFICATION OF THE MICRO-MECHANICS-BASED REDUCED ORDER MODEL

In this section, the presented stochastic M-T process, whose inputs have been stochastically identified in Section 3.4 by inverse analysis of the SVE realizations, is numerically verified with respect to the results obtained by direct stochastic homogenization in Section 2.3. First we compare the cumulative distributions of the stochastic M-T apparent elasticity tensor $\hat{\mathbb{C}}_{\text{M}}$ entries to the ones of the apparent elasticity tensor $\mathbb{C}_{\text{M}}$ directly obtained by computational homogenization. Then we compare the macro-scale stress distribution in a ply realization transversely loaded.

Although, knowing the entries of $\mathcal{V}_{\text{M-T}}$ from Section 3.4.2, we could build a generator of $\hat{\mathbb{C}}_{\text{M}}$, which will be done in the next section, for the sake of comparison and in order to avoid a possible bias from the generator, we reproduce here an apparent elasticity tensor $\hat{\mathbb{C}}_{\text{M}}$ from each $\mathbb{C}_{\text{M}}$ realization as follows

- For a given realization of $\mathbb{C}_{\text{M}}$ with a known v_{I}, we solve the optimization problem stated by Eqs. (34) and (38) to obtain the corresponding material parameters θ, γ, $\hat{E}_0$ and $\hat{\nu}_0$ of the M-T model.
- Using γ, $\hat{E}_0$ and $\hat{\nu}_0$ together with v_{I} and $\hat{\mathbb{C}}_{\text{I}}(\hat{E}_{\text{I}}^{\text{L}})$, the corresponding $\hat{\mathbb{C}}_{\text{M}}^{\text{L}}$ is evaluated through Eqs. (27) and (28).
- By using θ and the rotation Eq. (33), $\hat{\mathbb{C}}_{\text{M}}^{\text{L}}$ is rotated to the global coordinates, leading to $\hat{\mathbb{C}}_{\text{M}}$.

4.1. Comparison of meso-scale apparent property distributions

We first compare the cumulative distributions of the stochastic M-T apparent elasticity tensor $\hat{\mathbb{C}}_{\text{M}}$ entries to the ones of the apparent elasticity tensor $\mathbb{C}_{\text{M}}$ directly obtained by computational homogenization. By performing the reproduction process previously described on all the realizations of $\mathbb{C}_{\text{M}}$, the same number of $\hat{\mathbb{C}}_{\text{M}}$ is obtained, and the matrix form $\hat{\mathcal{C}}_{\text{M}}$ of the latter can also be represented by 13 random variables just as for $\mathcal{C}_{\text{M}}$, see Eq. (18).

Figure 9 compares the cumulative distributions of the 13 entries of $\mathcal{C}_{\text{M}}$ and $\hat{\mathcal{C}}_{\text{M}}$. A good agreement can be seen between the corresponding entries of $\mathcal{C}_{\text{M}}$ and the M-T reproduction $\hat{\mathcal{C}}_{\text{M}}$, at the exception of the entry $\hat{\mathcal{C}}_{\text{M66}}$ which is less accurate, see Fig 9(c). For this entry $\hat{\mathcal{C}}_{\text{M66}}$, its relative error is computed by

$$\text{err} = \frac{|\mathcal{C}_{\text{M66}} - \hat{\mathcal{C}}_{\text{M66}}|}{|\mathcal{C}_{\text{M66}}|}\,, \tag{42}$$

and reported statistically in Fig. 10. It can be seen that more than 50% of the samples have a relative error lower than 0.05 and that more than 90% of the samples have a relative error lower than

Prepared using nmeauth.cls
DOI: 10.1002/nme

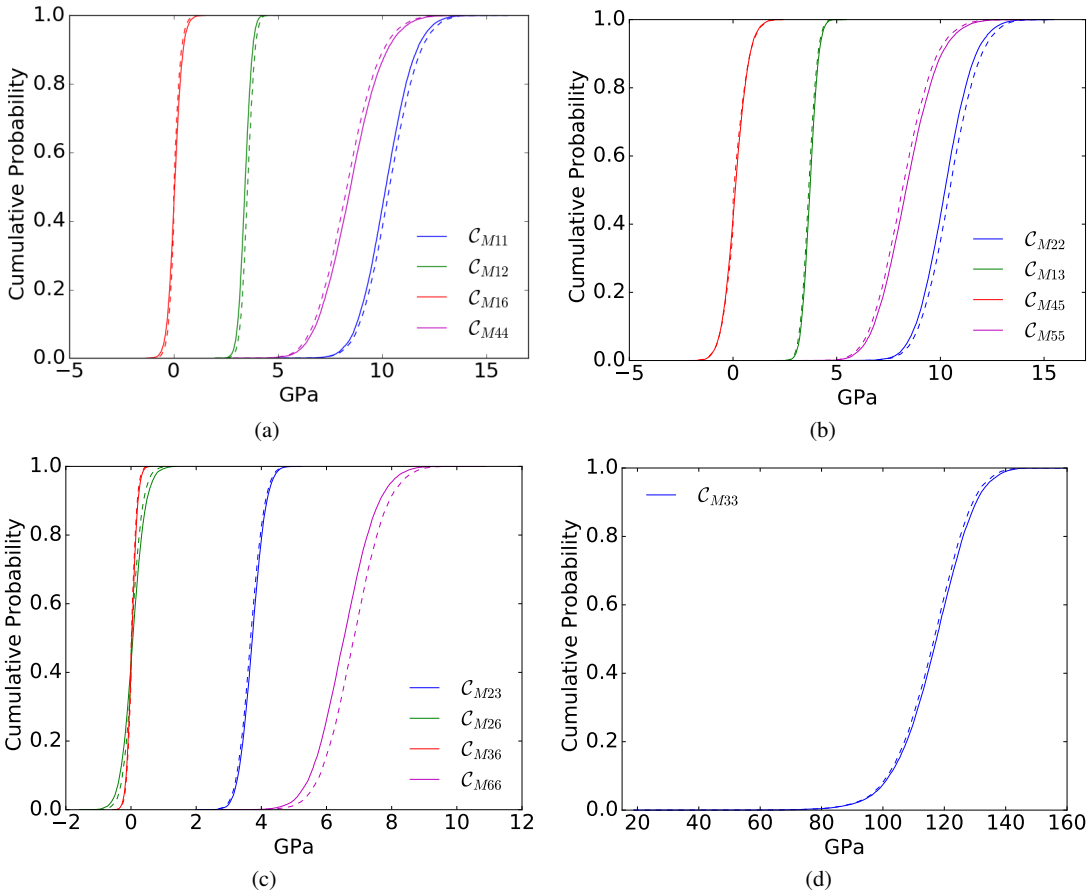

Figure 9. Cumulative distributions of entries of $\mathcal{C}_{\mathrm{M}}$ (solid lines) and of $\hat{\mathcal{C}}_{\mathrm{M}}$ (dashed lines).

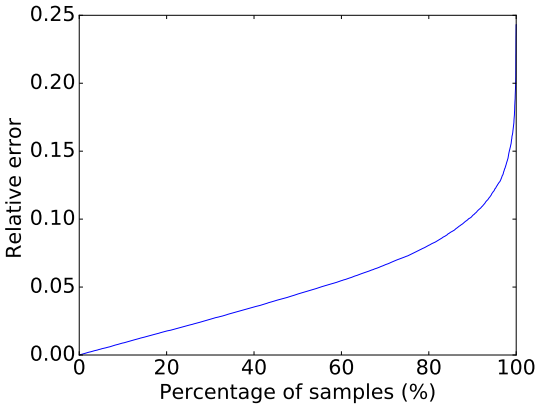

Figure 10. The percentage of samples which have a relative error lower than the value given by the vertical coordinate.

0.1, which remains acceptable for computational analyzes since the shearing in the cross-section is usually not the dominant response mode.

DOI: 10.1002/nme

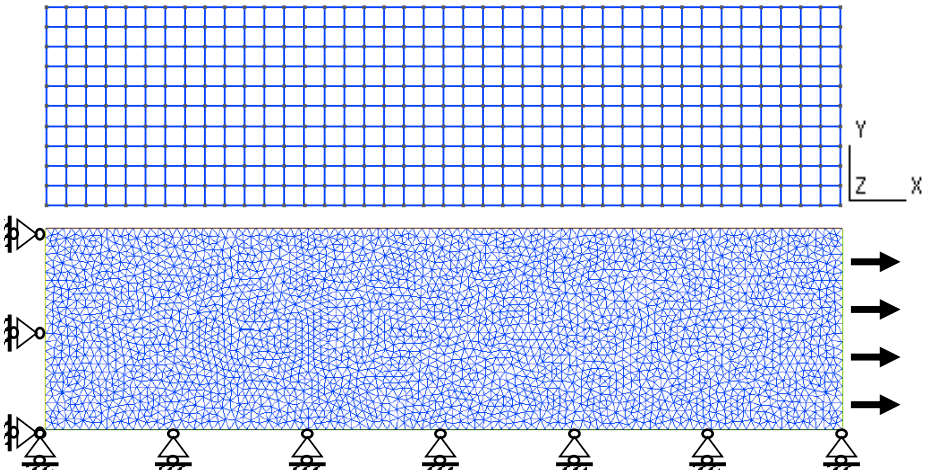

Figure 11. Tensile stochastic finite element analysis: discretizations of the random field (top) and of the finite element structure (bottom).

4.2. Verification of a macro-stress analysis of a tensile test realization

A tensile test is now performed on a ply cross-section realization by using the SFEM. A composite cross-section of $1000 \times 250\mu\text{m}^2$ is loaded in the transverse direction with plane strain condition along the z-direction and plane stress condition along the y-direction. The random field of the material properties is discretized into squares of $25 \times 25\mu\text{m}^2$, and the material properties of each square are independent of the properties in the neighboring squares [25]. In order to avoid a strong contrast of material properties, which may lead to an artificial stress concentration, smooth-step functions are used to describe the transition of material properties at the internal boundaries of the random field discretization [25]. The discretizations of the random field and of the finite element are shown in Fig. 11 along with the boundary and loading conditions that are applied on the structure. We successively consider two random material properties fields, which are

- The homogenized meso-scale properties $\mathbb{C}_{\text{M}}$ obtained from computational homogenization;
- The stochastic M-T apparent elasticity tensors $\hat{\mathbb{C}}_{\text{M}}$, which are reproduced from each $\mathbb{C}_{\text{M}}$ realization.

The macro-stress distributions $\sigma_{\text{M}xx}$ of the tensile test obtained with the two kinds of random material properties, random $\mathbb{C}_{\text{M}}$ and the corresponding $\hat{\mathbb{C}}_{\text{M}}$, are compared in Fig. 12 at the average loading strain $\varepsilon_{\text{M}_{xx}} = 7.2 \times 10^{-3}$. It can be seen that using $\hat{\mathbb{C}}_{\text{M}}$, Fig. 12(b), preserves the same level of uncertainty information as using $\mathbb{C}_{\text{M}}$, Fig. 12(a), in a stochastic multiscale analysis.

According to the comparisons of cumulative distributions, Fig. 9, the error study, Fig. 10, and the macro-scale stress distribution of a tensile test, it can be concluded that the presented stochastic M-T model is an accurate ROM. Indeed, by using the random vector $\mathcal{V}_{\text{M-T}} = [v_{\text{I}}, \theta, \gamma, \hat{E}_0, \hat{\nu}_0]^{\text{T}}$ in the M-T model, the apparent elastic properties of SVEs can be reproduced in an accurate way.

DOI: 10.1002/nme

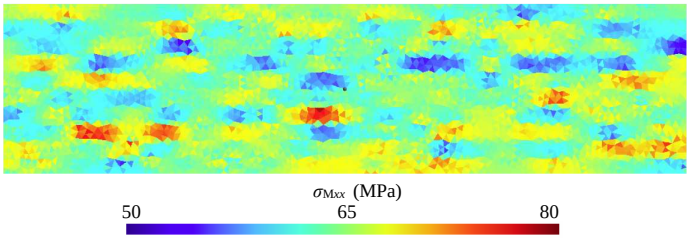

(a) Analysis with random $\mathbb{C}_{\mathrm{M}}$

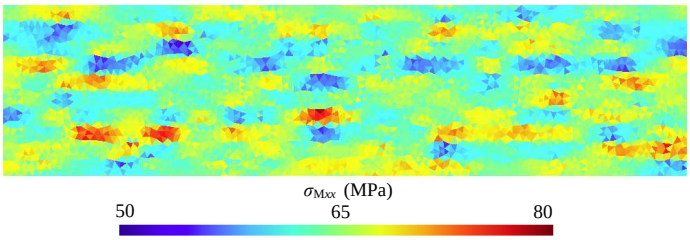

(b) Analysis with reproduced $\hat{\mathbb{C}}_{\mathrm{M}}$

Figure 12. Macro-stress $\sigma_{\mathrm{M}_{xx}}$ distributions in the $1000 \times 250\mu\mathrm{m}^2$ cross-section under transverse loading for an average loading strain $\varepsilon_{\mathrm{M}_{xx}} = 7.2 \times 10^{-3}$.

5. APPLICATION OF THE MICRO-MECHANICS REDUCED ORDER MODEL TO STOCHASTIC FINITE ELEMENT METHOD

In Section 2 the statistical homogenized behavior of UD composites has been analyzed by performing a stochastic homogenization of SVEs. In particular it has been shown in Section 2.4.2 that the resulting apparent elasticity tensors can be used to conduct a PCA and an order reduction. However, in order to keep micro-structure information in the ROM, and with a view to the extension to the nonlinear behavior, we have developed a stochastic M-T model in Section 3. In particular, it has been shown that by using the random vector $\mathcal{V}_{\text{M-T}} = [v_{\mathrm{I}}, \theta, \gamma, \hat{E}_0, \hat{\nu}_0]^{\mathrm{T}}$ in the M-T model, the apparent elastic properties of SVEs can be reproduced in an accurate way. However this random vector cannot be reduced anymore without loosing accuracy. In this section, we build a generator of the random vector $\mathcal{V}_{\text{M-T}}$ in order to conduct SFEM analyzes using the stochastic M-T model as micro-mechanics ROM.

5.1. Random meso-scale material properties generation

Meso-scale material properties are obtained by a two-step process:

- The random vector $\mathcal{V}_{\text{M-T}}$ is generated with its empirical distribution which is acquired based on the inverse study of 12740 realizations of $\mathbb{C}_{\mathrm{M}}$. In Section 3.4.2, it has been shown that the five random variables, $v_{\mathrm{I}}, \theta, \gamma, \hat{E}_0$ and $\hat{\nu}_0$, of the random vector $\mathcal{V}_{\text{M-T}}$ are not independent to each others. Therefore, pseudo-random samples of dependent random variables are generated by using their copula [42]. We need to note that the required number of realizations to construct an accurate empirical copula depends on the number of dependent random variables or on the order of $\mathcal{V}_{\text{M-T}}$: the more dependent random variables are involved, the more realizations are needed. This explains the reason of using more than 12000 realizations in this work, although

DOI: 10.1002/nme

the statistical convergence of $\mathbb{C}_{\mathrm{M}}$ has already been achieved after 3000 realizations, see Fig. 4.

- From the generated v_{I}, γ, $\hat{E}_0$ and $\hat{\nu}_0$ and the constant tensor $\hat{\mathbb{C}}_{\mathrm{I}}(\hat{E}_{\mathrm{I}}^{\mathrm{L}})$, the $\hat{\mathbb{C}}_{\mathrm{M}}^{\mathrm{L}}$ can be computed using the M-T model, *i.e.* through Eqs. (27) and (28) and then rotated to obtain $\hat{\mathbb{C}}_{\mathrm{M}}$ using the generated θ and Eq. (33).

In a SFEM analysis, the first step is an off-line process and the $\mathcal{V}_{\text{M-T}}$ realizations are used as material inputs of the SFEM. The second step can also be an off-line process in the context of linear finite element analyzes, but with a view to nonlinear studies it is embedded in the finite-element as a material law.

In order to assess the accuracy of the generation process, we generate 1000 random samples of $\hat{\mathbb{C}}_{\mathrm{M}}$. The entries of the generated samples are plotted in 2D in Fig. 13 to study their distributions and dependencies. One thousand realizations obtained from direct computational homogenizations are also plotted in Fig. 13 to serve as a reference. Only 1000 generated samples are considered for a better visualization. Since, $\mathbb{C}_{\mathrm{M}}$ has 13 random entries, it is not possible to show all the joint distributions between any two entries, so only part of the information is presented in Fig. 13. A good agreement in the joint distributions can be seen between the generated samples and their references in most of the cases, Figs. 13(a)-13(f). A lower accuracy is observed in Fig. 13(g) as expected according to the study in Section 4.1, since the stochastic M-T model provides a lower accuracy for $\mathcal{C}_{\mathrm{M66}}$; Fig. 13(h) also falls short of accuracy. However, the values of these entries are much lower than the other entries, and their effects in macro-scale analyzes are limited.

5.2. SFEM analysis of a ply under bending

In order to illustrate the applicability of the stochastic MT in the context of SFEM, we submit a composite cross-section of $875 \times 250\mu\mathrm{m}^2$ to a three-point bending test, see Fig. 14. Plane-strain conditions are assumed along the fiber direction, *i.e.* along the z-direction. A displacement δ is applied at the upper mid-length resulting in a loading force F along the y-direction.

The random field and finite element discretizations are illustrated in Fig. 14. In order to improve the efficiency of the SFEM analysis, the random field uses two different domain sizes: On the one hand, the random field of material properties is discretized into domains of $25 \times 25 \times 1\mu\mathrm{m}^3$ in the middle of the cross-section; On the other hand, the random field of material properties is discretized into domains of $125 \times 125 \times 1\mu\mathrm{m}^3$ at both extremities of the cross-section. The $25 \times 25 \times 1\mu\mathrm{m}^3$-domain size corresponds to that of the SVE studied in Section 2.3, so that the random vector $\mathcal{V}_{\text{M-T}}$ can be directly used as input of the M-T model. However, for the $125 \times 125 \times 1\mu\mathrm{m}^3$-domain size, proceeding as such would over-estimate the uncertainties since the random vector $\mathcal{V}_{\text{M-T}}$ was defined for a stochastic content of SVE of size $25 \times 25 \times 1\mu\mathrm{m}^3$. Therefore, relying on the fact that all the $25 \times 25 \times 1\mu\mathrm{m}^3$-SVEs are independently generated micro-structures, and that their spatial correlation does no have to be considered, see discussion in [25], we perform a two-step stochastic homogenization: 25 random vector $\mathcal{V}_{\text{M-T}}$ are generated for each domain of size $125 \times 125 \times 1\mu\mathrm{m}^3$ and a computational homogenization is performed on the latter to extract a $\mathbb{C}_{\mathrm{M}}$ realization. The relevance of the 2-step computational homogenization to capture the stochastic content with accuracy was discussed in [25]. Note that we could also have performed the inverse stochastic identification of the M-T model after having performed the computational homogenization on the

DOI: 10.1002/nme

$125 \times 125 \times 1 \mu\text{m}^3$-SVE in order to be able to generate the two kinds of random vectors $\mathcal{V}_{\text{M-T}}$ for the two different SVE sizes, and such an approach will be used in nonlinear analyzes for which offline computation of the material response is not possible. Monte-Carlo simulations can then be conducted on the 3-point bending sample to study the effect of material uncertainties on the structural response.

Figure 15 reports the histograms of the homogenized tensile stress $\sigma_{\text{M}xx}$ at the mid-length lower face reached in each sample and the applied loading F per unit thickness for a maximum displacement $\delta = 8.0\mu$m at the loading point. Note that $\sigma_{\text{M}xx}$ is not the maximum stress reached in the different phases of the composite material. This figure shows that the stochastic Mori-Tanaka model predicts uncertainties in the structural response and in particular in the maximum tensile stress $\sigma_{\text{M}xx}$ of the composite ply, which explains the discrepancy observed during failure analysis of composites.

In order to assess the performance of the numerical methodology, we can sort the computational times as follows

- The largest computation time results from the computational homogenization of the SVEs as performed in Section 2. A typical computational time ranges from 1.5 s for a SVE length $l_{\text{SVE}} = 25\,\mu$m to 1250 s for a SVE length of $l_{\text{SVE}} = 125\,\mu\text{m}^{\ddagger}$, per SVE realization, with more than 10000 realization required.
- The inverse identification process developed in Section 3 requires a fraction of second per SVE, independently of the SVE length. Note that both the SVE resolution and the inverse identification process can be achieved in parallel easily since the SVE realizations are independent from each other.
- Building the copula from the 12740 realizations of $\hat{\mathbb{C}}_{\text{M}}$ obtained though the inverse identification process requires around 2 s and is one-time operation. These latter three operations are off-line operations.
- Finally, the time requires to generate a random vector field $\mathcal{V}_{\text{M-T}}$ for one realization of the SFEM problem illustrated in Fig. 14 is about 70 s, time which includes the 2-step homogenization performed for $125\,\mu$m-long grid elements.

6. CONCLUSIONS

A micro-mechanics based order reduction procedure was presented in this work to reduce the number of random variables required to describe the random apparent material properties of SVEs. The presented procedure is based on the mean-field homogenization method, especially the Mori-Tanaka model, and focuses on inclusions reinforced matrix composites, in particular elastic UD fiber reinforced matrix.

A reduced number of full-field simulations of SVE realizations was required to define the statistical apparent or homogenized meso-scale properties, which can be represented by a random vector $\mathcal{V}$ –here the anisotropic elastic tensor. Then, an inverse stochastic identification process was

[‡]As explained, in this paper we had recourse to a 2-step homogenization for those larger SVEs in order to avoid this extra cost

DOI: 10.1002/nme

performed from the apparent elastic properties in order to define the random vector $\mathcal{V}_{\text{M-T}}$ of the effective elastic properties of phases and micro-structure information of the Mori-Tanaka model. In order to conduct SFEM, a generator of the random vector $\mathcal{V}_{\text{M-T}}$ was constructed using the copula method.

We have then compared the meso-scale stochastic properties obtained directly by stochastic computational homogenization and by the stochastic Mori-Tanaka model, and we have shown that the stochastic Mori-Tanaka model respects the cumulative distribution and dependence of the anisotropic homogenized elasticity tensor components.

In this work, the uncertain material response was propagated from the micro-scale to the macro-scale under a linear elastic assumption by combining the generator of random vector $\mathcal{V}_{\text{M-T}}$ of the effective elastic properties of phases and micro-structure information of the Mori-Tanaka model and SFEM. Although the copula method could also have been used to build a generator of the random vector $\mathcal{V}$ obtained by the stochastic computational homogenization, the number of realizations required as input to construct this empirical copula is an exponential function of the number of random variables involved. A dimension reduction should thus be used using the PCA analysis. It was shown in this work that the presented micro-mechanics procedure has the same order reduction effect as applying PCA on $\mathcal{V}$ in which case the number of needed random variables is reduced from 13 to 5. However, the micro-mechanics based order reduction is more prospective than the PCA for a future extension to nonlinear behaviors. Indeed, when considering plasticity and/or damage and/or failure, a direct description of the meso-scale response cannot be stated in the form of a single material tensor. Therefore, the responses obtained from computational homogenizations of SVEs will not only demand a complex material model to be defined, but also a lot of material parameters, which are surely to be random variables, to be inferred. Since the stochastic Mori-Tanaka model is based on micro-mechanics and takes the information of the micro-structure into account, it is expected to simplify the stochastic description of nonlinear behaviors in a future work. In particular, in the case of damaging behavior, the micro-mechanics model will be based on the non-local incremental-secant Mori-Tanaka model, which avoids mesh dependency at the macro-scale through the definition of a characteristic length scale [37].

ACKNOWLEDGMENT

The research has been funded by the Walloon Region under the agreement no 1410246-STOMMMAC (CT-INT 2013-03-28) in the context of the M-ERA.NET Joint Call 2014.

DOI: 10.1002/nme

A. TENSORIAL OPERATIONS AND NOTATIONS

- Dots and colons are used to indicate tensor products contracted over one and two indices respectively:

$$\begin{aligned} \boldsymbol{u}\cdot\boldsymbol{v} &= u_i v_i, & (\boldsymbol{a}\cdot\boldsymbol{u})_i &= a_{ij}u_j\,; \\ (\boldsymbol{a}\cdot\boldsymbol{b})_{ij} &= a_{ik}b_{kj}, & \boldsymbol{a}:\boldsymbol{b} &= a_{ij}b_{ji}\,; \\ (\mathbb{C}:\boldsymbol{a})_{ij} &= \mathbb{C}_{ijkl}a_{lk}, & (\mathbb{C}:\mathbb{D})_{ijkl} &= \mathbb{C}_{ijmn}\mathbb{D}_{nmkl}\,. \end{aligned} \tag{43}$$

- Dyadic products are designated by $\otimes$:

$$(\boldsymbol{u}\otimes\boldsymbol{v})_{ij} = u_i v_j, \quad (\boldsymbol{a}\otimes\boldsymbol{b})_{ijkl} = a_{ij}b_{kl}\,. \tag{44}$$

- Symbols $\mathbf{1}$ and $\mathbb{I}$ designate the second- and fourth-order symmetric identity tensors respectively:

$$\mathbf{1}_{ij} = \delta_{ij}, \quad \mathbb{I}_{ijkl} = \frac{1}{2}(\delta_{ik}\delta_{jl} + \delta_{il}\delta_{jk})\,, \tag{45}$$

  where $\delta_{ij} = 1$ if $i = j$, $\delta_{ij} = 0$ if $i \neq j$.

B. CONSTRAINT AND KINEMATIC MATRICES FOR PBCS

Using Eq. (6) allows relating the fluctuation $\boldsymbol{u}'$ to the nodal unknowns on the boundary gathered in the nodal vector $\mathbf{u}_{\mathrm{m}}^{\pm}$, where the superscript "$\pm$" refers to all the boundary nodes, and Eq. (16) becomes

$$\mathbf{u}_{\mathrm{m}}^{\pm} - \mathbf{S}\mathcal{E}_{\mathrm{M}} - \mathbf{A}\mathbf{u}_{\mathrm{m}}^{a} = 0\,, \tag{46}$$

where $\mathbf{A}$ is the constraint coefficients matrix constructed from the values of the interpolation bases $N_k^i(\boldsymbol{x}^-)$, where $\boldsymbol{a}_j^i$ with $j = 1, ..., n+1$ are gathered under the nodal vector $\mathbf{u}_{\mathrm{m}}^{a}$ of size $9(n+1)$ (3 surfaces $\partial\omega^i$ and three degrees of freedom per term $\boldsymbol{a}_j^i$), and where $\mathbf{S}$ is the assembly matrix of boundary nodal positions $\mathbf{x}^{\pm}$ from $\boldsymbol{x}^{\mathrm{ref}}$

$$\mathbf{S}_{3n^b\times 9} = \begin{bmatrix} \mathbf{x}_x^{\pm T} & 0_{1\times n^b} & 0_{1\times n^b} \\ \mathbf{x}_y^{\pm T} & 0_{1\times n^b} & 0_{1\times n^b} \\ \mathbf{x}_z^{\pm T} & 0_{1\times n^b} & 0_{1\times n^b} \\ 0_{1\times n^b} & \mathbf{x}_x^{\pm T} & 0_{1\times n^b} \\ 0_{1\times n^b} & \mathbf{x}_y^{\pm T} & 0_{1\times n^b} \\ 0_{1\times n^b} & \mathbf{x}_z^{\pm T} & 0_{1\times n^b} \\ 0_{1\times n^b} & 0_{1\times n^b} & \mathbf{x}_x^{\pm T} \\ 0_{1\times n^b} & 0_{1\times n^b} & \mathbf{x}_y^{\pm T} \\ 0_{1\times n^b} & 0_{1\times n^b} & \mathbf{x}_z^{\pm T} \end{bmatrix}^T, \tag{47}$$

DOI: 10.1002/nme

where n^b is the number of boundary nodes.

The set of Eqs. (13) is then rewritten by considering as degrees of freedom $\mathbf{u}_m = [\mathbf{u}_{\mathrm{m}}^{I^T} \ \mathbf{u}_{\mathrm{m}}^{\pm^T} \ \mathbf{u}_{\mathrm{m}}^{a^T}]^T$, where $\mathbf{u}_{\mathrm{m}}^I$ are the nodal degrees of freedom of the n^I nodes not lying on the boundary $\partial\omega$. The matrices thus read $\mathbf{C} = \left[0_{3n^b\times 3*n^I} \quad \mathbf{I}_{3n^b\times 3n^b} \quad -\mathbf{A}_{3n^b\times 9(n+1)}\right]$ and $\mathbf{K}_{\mathrm{m}} = \begin{bmatrix} \mathbf{K}_m^{II} & \mathbf{K}_m^{I\pm} & 0_{3n^I\times 9(n+1)} \\ \mathbf{K}_m^{\pm I} & \mathbf{K}_m^{\pm\pm} & 0_{3n^b\times 9(n+1)} \\ 0_{9(n+1)\times 3n^I} & 0_{9(n+1)\times 3n^b} & 0_{9(n+1)\times 9(n+1)} \end{bmatrix}$, where the micro-scale BVP stiffness matrix has been decomposed in terms of internal and boundary degrees of freedom. More details about the implementation can be found in [45].

C. ESHELBY'S TENSOR FOR AN ELLIPTIC CYLINDER IN AN ISOTROPIC MEDIUM

The Eshelby's tensor satisfies minor symmetries,

$$\mathbb{S}_{ijkl} = \mathbb{S}_{jikl} = \mathbb{S}_{ijlk} \quad i,j,k,l = 1,2,3\,. \tag{48}$$

However, it does not satisfy major symmetry. For an elliptic cylinder of cross-section semi axes a and b, with $a \to b$, a and b correspond to the directions $1 \to 2$ and the longitudinal direction of the cylinder with 3. In an isotropic medium, the nonzero terms of the Eshelby's tensor $\mathbb{S}$ read [50]

$$\begin{aligned}
\mathbb{S}_{1111} &= \frac{1}{2(1-\nu)}\left[\frac{b^2+2ab}{(a+b)^2} + (1-2\nu)\frac{b}{a+b}\right] \\
\mathbb{S}_{2222} &= \frac{1}{2(1-\nu)}\left[\frac{a^2+2ab}{(a+b)^2} + (1-2\nu)\frac{a}{a+b}\right] \\
\mathbb{S}_{1122} &= \frac{1}{2(1-\nu)}\left[\frac{b^2}{(a+b)^2} - (1-2\nu)\frac{b}{a+b}\right] \\
\mathbb{S}_{2233} &= \frac{1}{2(1-\nu)}\frac{2\nu a}{a+b} \\
\mathbb{S}_{2211} &= \frac{1}{2(1-\nu)}\left[\frac{a^2}{(a+b)^2} - (1-2\nu)\frac{a}{a+b}\right] \\
\mathbb{S}_{1212} &= \frac{1}{2(1-\nu)}\left[\frac{a^2+b^2}{2(a+b)^2} + \frac{(1-2\nu)}{2}\right] \\
\mathbb{S}_{1133} &= \frac{1}{2(1-\nu)}\frac{2\nu b}{a+b} \\
\mathbb{S}_{2323} &= \frac{a}{2(a+b)} \\
\mathbb{S}_{3131} &= \frac{b}{2(a+b)}\,,
\end{aligned} \tag{49}$$

where ν is the Poisson ratio of the medium (here the matrix).

REFERENCES

Prepared using nmeauth.cls
DOI: 10.1002/nme

1. Kanouté P, Boso DP, Chaboche JL, Schrefler BA. Multiscale methods for composites: A review. *Archives of Computational Methods in Engineering* Mar 2009; **16**(1):31–75, doi:10.1007/s11831-008-9028-8. URL https://doi.org/10.1007/s11831-008-9028-8.
2. Noels L, Wu L, Adam L, Seyfarth J, Soni G, Segurado J, Laschet G, Chen G, Lesueur M, Lobos M, *et al.*. Effective properties. *Handbook of Software Solutions for ICME*. Wiley-VCH Verlag GmbH & Co. KGaA, 2016; 433–485, doi:10.1002/9783527693566.ch6. URL http://dx.doi.org/10.1002/9783527693566.ch6.
3. Matous K, Geers MG, Kouznetsova VG, Gillman A. A review of predictive nonlinear theories for multiscale modeling of heterogeneous materials. *Journal of Computational Physics* 2017; **330**(Supplement C):192 – 220, doi:10.1016/j.jcp.2016.10.070.
4. Feyel F. Multiscale fe2 elastoviscoplastic analysis of composite structures. *Computational Materials Science* 1999; **16**(1):344 – 354, doi:http://dx.doi.org/10.1016/S0927-0256(99)00077-4. URL http://www.sciencedirect.com/science/article/pii/S0927025699000774.
5. Michel J, Moulinec H, Suquet P. Effective properties of composite materials with periodic microstructure: a computational approach. *Computer Methods in Applied Mechanics and Engineering* 1999; **172**(1):109 – 143, doi:http://dx.doi.org/10.1016/S0045-7825(98)00227-8. URL http://www.sciencedirect.com/science/article/pii/S0045782598002278.
6. Terada K, Hori M, Kyoya T, Kikuchi N. Simulation of the multi-scale convergence in computational homogenization approaches. *International Journal of Solids and Structures* 2000; **37**(16):2285 – 2311, doi:http://dx.doi.org/10.1016/S0020-7683(98)00341-2. URL http://www.sciencedirect.com/science/article/pii/S0020768398003412.
7. Kouznetsova V, Brekelmans WAM, Baaijens FPT. An approach to micro-macro modeling of heterogeneous materials. *Computational Mechanics* Jan 2001; **27**(1):37–48, doi:10.1007/s004660000212. URL https://doi.org/10.1007/s004660000212.
8. Miehe C. Strain-driven homogenization of inelastic microstructures and composites based on an incremental variational formulation. *International Journal for Numerical Methods in Engineering* 2002; **55**(11):1285–1322, doi:10.1002/nme.515. URL http://dx.doi.org/10.1002/nme.515.
9. Yvonnet J, He QC. The reduced model multiscale method (r3m) for the non-linear homogenization of hyperelastic media at finite strains. *Journal of Computational Physics* 2007; **223**(1):341 – 368, doi:https://doi.org/10.1016/j.jcp.2006.09.019. URL http://www.sciencedirect.com/science/article/pii/S0021999106004402.
10. Hernández J, Oliver J, Huespe A, Caicedo M, Cante J. High-performance model reduction techniques in computational multiscale homogenization. *Computer Methods in Applied Mechanics and Engineering* 2014; **276**:149 – 189, doi:https://doi.org/10.1016/j.cma.2014.03.011. URL http://www.sciencedirect.com/science/article/pii/S0045782514000978.
11. Soldner D, Brands B, Zabihyan R, Steinmann P, Mergheim J. A numerical study of different projection-based model reduction techniques applied to computational homogenisation. *Computational Mechanics* Oct 2017; **60**(4):613–625, doi:10.1007/s00466-017-1428-x. URL https://doi.org/10.1007/s00466-017-1428-x.
12. Michel JC, Suquet P. Nonuniform transformation field analysis: a reduced model for multiscale nonlinear problems in solid mechanics. *Multiscale Modelling in Solid Mechanics - Computational Approaches*, Galvanetto U, Aliabadi F (eds.). Imperial College Press, Imperial College Press, London., 2009; 159–206. URL https://hal.archives-ouvertes.fr/hal-00367772, iSBN: 978-1-84816-307-2.
13. Michel JC, Suquet P. A model-reduction approach in micromechanics of materials preserving the variational structure of constitutive relations. *Journal of the Mechanics and Physics of Solids* 2016; **90**:254 – 285, doi:https://doi.org/10.1016/j.jmps.2016.02.005. URL http://www.sciencedirect.com/science/article/pii/S0022509616300928.
14. Wirtz D, Karajan N, Haasdonk B. Surrogate modeling of multiscale models using kernel methods. *International Journal for Numerical Methods in Engineering* 2015; **101**(1):1–28, doi:10.1002/nme.4767. URL http://dx.doi.org/10.1002/nme.4767.
15. Perrin G, Soize C, Duhamel D, Funfschilling C. Identification of polynomial chaos representations in high dimension from a set of realizations. *SIAM Journal on Scientific Computing* 2012; **34**(6):A2917–A2945, doi:10.1137/11084950X. URL https://doi.org/10.1137/11084950X.
16. Ostoja-Starzewski M, Wang X. Stochastic finite elements as a bridge between random material microstructure and global response. *Computer Methods in Applied Mechanics and Engineering* 1999; **168**(14):35 – 49, doi:http://dx.doi.org/10.1016/S0045-7825(98)00105-4.
17. Ostoja-Starzewski M, Du X, Khisaeva ZF, Li W. Comparisons of the size of the representative volume element in elastic, plastic, thermoelastic, and permeable random microstructures. *International Journal for Multiscale Computational Engineering* 2007; **5**(2):73–82.

18. Salmi M, Fran cA, Bornert M, Fogli M. Apparent and effective mechanical properties of linear matrix-inclusion random composites: Improved bounds for the effective behavior. *International Journal of Solids and Structures* 2012; **49**(10):1195 – 1211, doi:https://doi.org/10.1016/j.ijsolstr.2012.01.018. URL http://www.sciencedirect.com/science/article/pii/S0020768312000340.
19. Trovalusci P, De Bellis ML, Ostoja-Starzewski M, Murrali A. Particulate random composites homogenized as micropolar materials. *Meccanica* Nov 2014; **49**(11):2719–2727, doi:10.1007/s11012-014-0031-x. URL https://doi.org/10.1007/s11012-014-0031-x.
20. Trovalusci P, Ostoja-Starzewski M, De Bellis ML, Murrali A. Scale-dependent homogenization of random composites as micropolar continua. *European Journal of Mechanics - A/Solids* 2015; **49**(0):396 – 407, doi: http://dx.doi.org/10.1016/j.euromechsol.2014.08.010.
21. Reccia E, De Bellis ML, Trovalusci P, Masiani R. Sensitivity to material contrast in homogenization of random particle composites as micropolar continua. *Composites Part B: Engineering* 2018; **136**:39 – 45, doi:https://doi.org/10.1016/j.compositesb.2017.10.017. URL http://www.sciencedirect.com/science/article/pii/S1359836817325088.
22. Stefanou G, Savvas D, Papadrakakis M. Stochastic finite element analysis of composite structures based on material microstructure. *Composite Structures* 2015; **132**:384 – 392, doi:http://dx.doi.org/10.1016/j.compstruct.2015.05.044. URL http://www.sciencedirect.com/science/article/pii/S0263822315004183.
23. Savvas D, Stefanou G, Papadrakakis M. Determination of rve size for random composites with local volume fraction variation. *Computer Methods in Applied Mechanics and Engineering* 2016; **305**:340 – 358, doi:http://dx.doi.org/10.1016/j.cma.2016.03.002. URL http://www.sciencedirect.com/science/article/pii/S0045782516300822.
24. Stefanou G, Savvas D, Papadrakakis M. Stochastic finite element analysis of composite structures based on mesoscale random fields of material properties. *Computer Methods in Applied Mechanics and Engineering* 2017; :–doi:https://doi.org/10.1016/j.cma.2017.08.002. URL http://www.sciencedirect.com/science/article/pii/S0045782517305868.
25. Wu L, Chung CN, Major Z, Adam L, Noels L. From sem images to elastic responses: a stochastic multiscale analysis of ud fiber reinforced composites. *Composite Structures* 2018; **189C**:206 – 227, doi: https://doi.org/10.1016/j.compstruct.2018.01.051.
26. Lucas V, Golinval JC, Paquay S, Nguyen VD, Noels L, Wu L. A stochastic computational multiscale approach; application to mems resonators. *Computer Methods in Applied Mechanics and Engineering* 2015; **294**:141 – 167, doi:http://dx.doi.org/10.1016/j.cma.2015.05.019. URL http://www.sciencedirect.com/science/article/pii/S0045782515001929.
27. Wu L, Lucas V, Nguyen VD, Golinval JC, Paquay S, Noels L. A stochastic multi-scale approach for the modeling of thermo-elastic damping in micro-resonators. *Computer Methods in Applied Mechanics and Engineering* 2016; **310**:802 – 839, doi:http://dx.doi.org/10.1016/j.cma.2016.07.042. URL http://www.sciencedirect.com/science/article/pii/S0045782516303930.
28. Pivovarov D, Steinmann P. Modified sfem for computational homogenization of heterogeneous materials with microstructural geometric uncertainties. *Computational Mechanics* 2016; **57**(1):123–147.
29. Fish J, Wu W. A nonintrusive stochastic multiscale solver. *International Journal for Numerical Methods in Engineering* 2011; **88**(9):862–879, doi:10.1002/nme.3201.
30. Clément A, Soize C, Yvonnet J. Computational nonlinear stochastic homogenization using a nonconcurrent multiscale approach for hyperelastic heterogeneous microstructures analysis. *International Journal for Numerical Methods in Engineering* 2012; **91**(8):799–824, doi:10.1002/nme.4293.
31. Yvonnet J, Monteiro E, He QC. Computational homogenization method and reduced database model for hyperelastic heterogeneous structures. *International Journal for Multiscale Computational Engineering* 2013; **11**(3):201–225.
32. Bessa M, Bostanabad R, Liu Z, Hu A, Apley DW, Brinson C, Chen W, Liu WK. A framework for data-driven analysis of materials under uncertainty: Countering the curse of dimensionality. *Computer Methods in Applied Mechanics and Engineering* 2017; **320**:633 – 667, doi:http://dx.doi.org/10.1016/j.cma.2017.03.037. URL http://www.sciencedirect.com/science/article/pii/S0045782516314803.
33. Mori T, Tanaka K. Average stress in matrix and average elastic energy of materials with misfitting inclusions. *Acta Metallurgica* 1973; **21**(5):571–574.
34. Wu L, Noels L, Adam L, Doghri I. A combined incremental-secant mean-field homogenization scheme with per-phase residual strains for elasto-plastic composites. *International Journal of Plasticity* 2013; **51**:80 – 102, doi:https://doi.org/10.1016/j.ijplas.2013.06.006. URL http://www.sciencedirect.com/science/article/pii/S0749641913001174.

DOI: 10.1002/nme

35. Yang S, Yu S, Ryu J, Cho JM, Kyoung W, Han DS, Cho M. Nonlinear multiscale modeling approach to characterize elastoplastic behavior of cnt/polymer nanocomposites considering the interphase and interfacial imperfection. *International Journal of Plasticity* 2013; **41**:124 – 146, doi:https://doi.org/10.1016/j.ijplas.2012.09.010. URL http://www.sciencedirect.com/science/article/pii/S0749641912001404.
36. Hoang TH, Guerich M, Yvonnet J. Determining the size of rve for nonlinear random composites in an incremental computational homogenization framework. *Journal of Engineering Mechanics* 2016; **142**(5):04016 018, doi: 10.1061/(ASCE)EM.1943-7889.0001057.
37. Wu L, Noels L, Adam L, Doghri I. An implicit-gradient-enhanced incremental-secant mean-field homogenization scheme for elasto-plastic composites with damage. *International Journal of Solids and Structures* 2013; **50**(24):3843 – 3860, doi:10.1016/j.ijsolstr.2013.07.022.
38. Wu L, Sket F, Molina-Aldareguia J, Makradi A, Adam L, Doghri I, Noels L. A study of composite laminates failure using an anisotropic gradient-enhanced damage mean-field homogenization model. *Composite Structures* 2015; **126**:246 – 264, doi:http://dx.doi.org/10.1016/j.compstruct.2015.02.070. URL http://www.sciencedirect.com/science/article/pii/S0263822315001580.
39. Alzebdeh K, Ostoja-Starzewski M. Micromechanically based stochastic finite elements: length scales and anisotropy. *Probabilistic Engineering Mechanics* 1996; **11**(4):205 – 214, doi:http://dx.doi.org/10.1016/0266-8920(96)00015-X. Third International Stochastic Structural Dynamics Conference.
40. Ghanem R, Spanos P. *Stochastic Finite Elements: A Spectral Approach*. Springer Verlag, 1991.
41. Lemaitre O, Knio O. *Spectral methods for uncertainty quantification - with applications to computational fluid dynamics*. Springer, 2010.
42. Strelen JC, Nassaj F. Analysis and generation of random vectors with copulas. *Proceedings of the 39th Conference on Winter Simulation: 40 Years! The Best is Yet to Come*, WSC '07, IEEE Press: Piscataway, NJ, USA, 2007; 488–496. URL http://dl.acm.org/citation.cfm?id=1351542.1351639.
43. Miehe C, Koch A. Computational micro-to-macro transitions of discretized microstructures undergoing small strains. *Archive of Applied Mechanics* 2002; **72**(4-5):300–317, doi:10.1007/s00419-002-0212-2.
44. Ainsworth M. Essential boundary conditions and multi-point constraints in finite element analysis. *Computer Methods in Applied Mechanics and Engineering* 2001; **190**(48):6323 – 6339, doi:http://dx.doi.org/10.1016/S0045-7825(01)00236-5. URL http://www.sciencedirect.com/science/article/pii/S0045782501002365.
45. Nguyen VD, Wu L, Noels L. Unified treatment of microscopic boundary conditions and efficient algorithms for estimating tangent operators of the homogenized behavior in the computational homogenization method. *Computational Mechanics* Mar 2017; **59**(3):483–505, doi:10.1007/s00466-016-1358-z. URL https://doi.org/10.1007/s00466-016-1358-z.
46. Peric D, de Souza Neto EA, Feijóo RA, Partovi M, Molina AJC. On micro-to-macro transitions for multi-scale analysis of non-linear heterogeneous materials: unified variational basis and finite element implementation. *International Journal for Numerical Methods in Engineering* 2010; **87**:149 – 170. URL http://dx.doi.org/10.1002/nme.3014.
47. Schröder J, Labusch M, Keip MA. Algorithmic two-scale transition for magneto-electro-mechanically coupled problems: Fe2-scheme: Localization and homogenization. *Computer Methods in Applied Mechanics and Engineering* 2016; **32**:253–280, doi:http://dx.doi.org/10.1016/j.cma.2015.10.005. URL http://www.sciencedirect.com/science/article/pii/S0045782515003242.
48. Nguyen VD, Béchet E, Geuzaine C, Noels L. Imposing periodic boundary condition on arbitrary meshes by polynomial interpolation. *Computational Materials Science* 2012; **55**(0):390 – 406, doi:10.1016/j.commatsci.2011.10.017. URL http://www.sciencedirect.com/science/article/pii/S0927025611005866.
49. Hill R. A self-consistent mechanics of composite materials. *Journal of the Mechanics and Physics of Solids* 1965; **13**(4):213 – 222, doi:DOI: 10.1016/0022-5096(65)90010-4.
50. Eshelby JD. The determination of the elastic field of an ellipsoidal inclusion, and related problems. *Proceedings of the Royal Society of London. Series A, Mathematical and Physical Sciences* 1957; **241**(1226):pp. 376–396.
51. Segurado J, Llorca J. A numerical approximation to the elastic properties of sphere-reinforced composites. *Journal of the Mechanics and Physics of Solids* 2002; **50**(10):2107 – 2121.
52. Szkely GJ, Rizzo ML, Bakirov NK. Measuring and testing dependence by correlation of distances. *Ann. Statist.* 12 2007; **35**(6):2769–2794, doi:10.1214/009053607000000505. URL http://dx.doi.org/10.1214/009053607000000505.

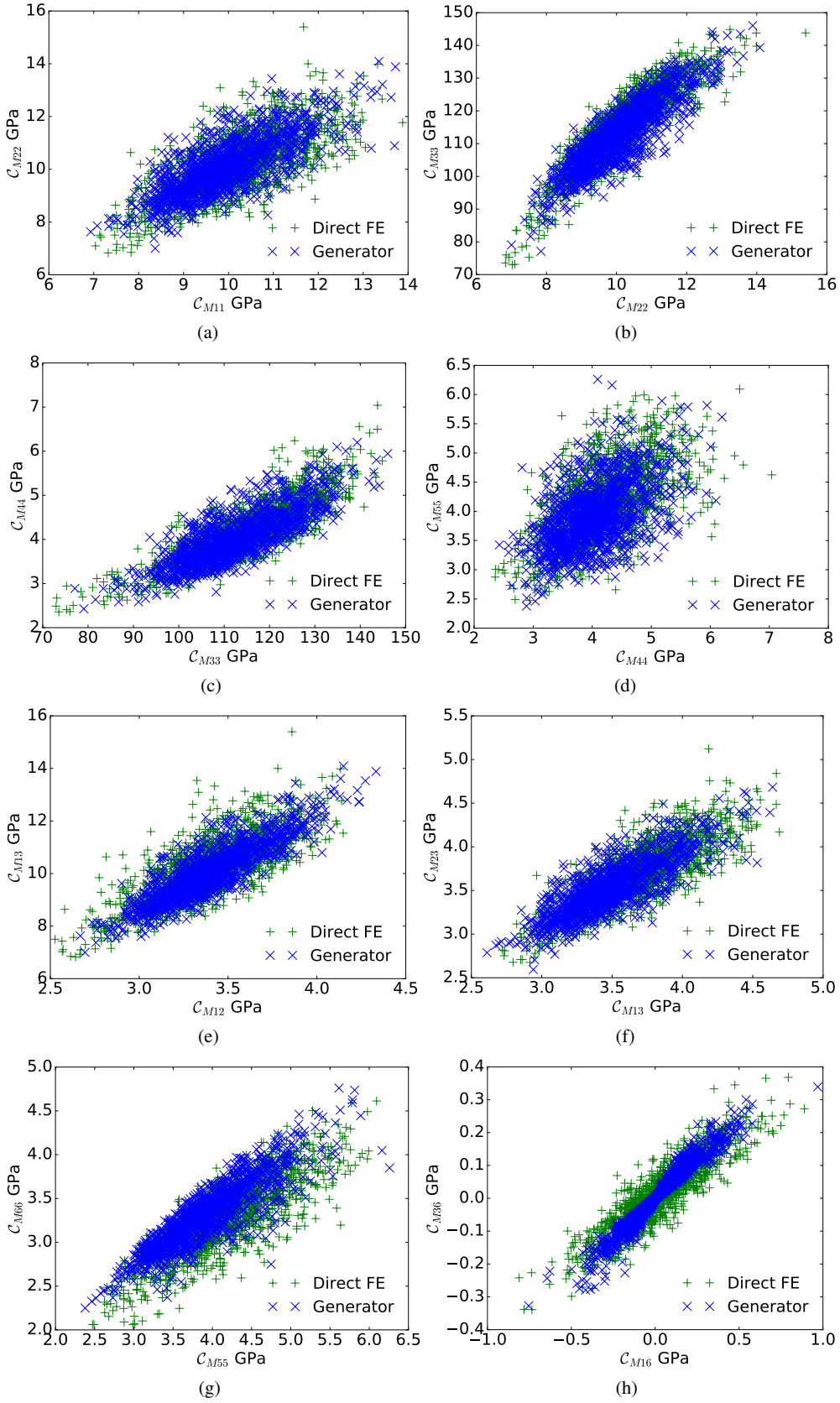

Figure 13. Comparison of the joint distributions of the homogenized elastic properties from computational homogenization and micro-mechanics-based generator.

Prepared using nmeauth.cls
DOI: 10.1002/nme

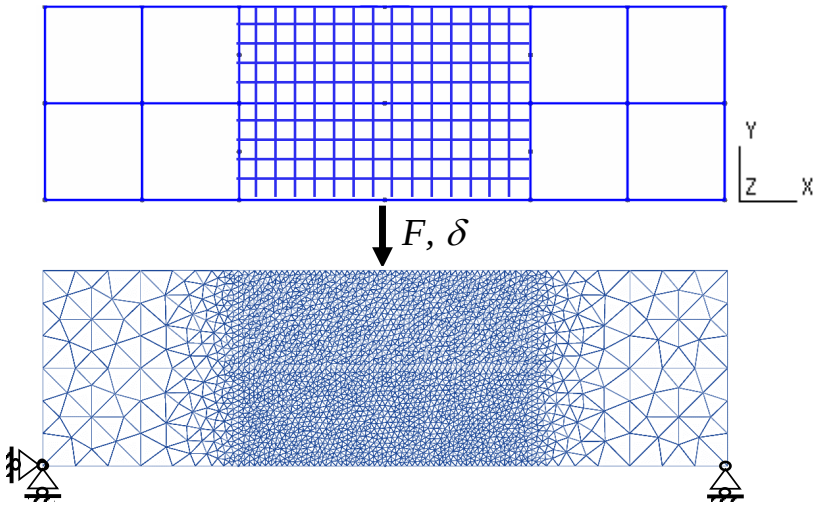

Figure 14. Stochastic finite element analysis of a ply under bending: discretizations of the random field (top) and of the finite element structure (bottom).

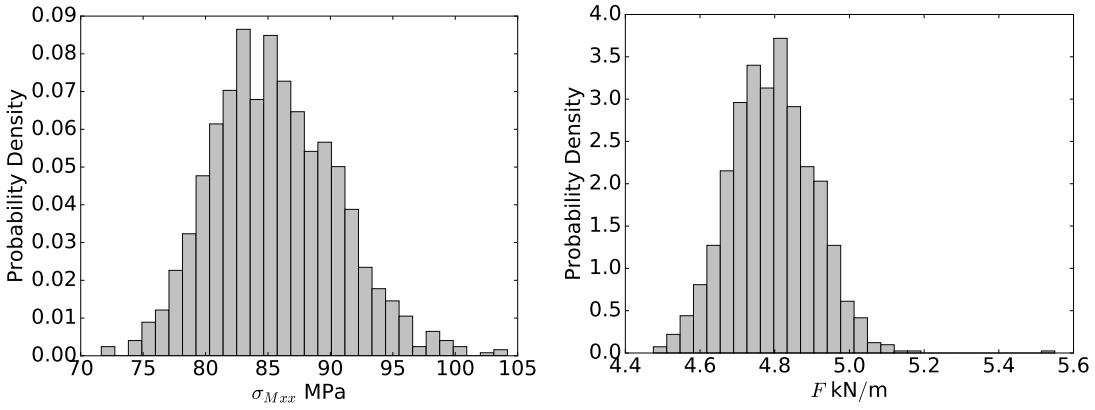

Figure 15. The histograms of the stochastic bending test (1141 samples) for a displacement $\delta = 8.0\mu$m: (a) The maximum tensile stress $\sigma_{\mathrm{M}xx}$ reached in each sample; and (b) The applied loading F per unit thickness.

DOI: 10.1002/nme